Large Area Avalanche Photodiode Gain Optimization for the APFEL ASIC Preamplifiers of the P̄ANDA Calorimeter

Bachelor thesis
by Kim Tabea Giebenhain
from Biebertal
August 22, 2019

Justus-Liebig University, Giessen
II. Institute of Physics

Abstract

In the course of this thesis, the optimum gain working point in terms of the maximum energy resolution for the LAAPDs which are to be used by the P̄ANDA electromagnetic calorimeter at the future FAIR-facility at the GSI in Darmstadt was determined. The LAAPD used was calibrated with cosmic myons in order to attribute a signal to the equivalent energy. To ensure a stable working environment, the time stability of the utilized LED-pulser was tested.

The linearity between the high-gain amplification branch and the low-gain branch of the APFEL ASIC was measured, which shows a high non-linearity even at relatively low energies. Furthermore, the gain characterization of the LAAPD was checked and the following behaviour was observed: The behaviour of the LAAPD amplification is dependent on whether or not they are operated under continuous illumination. With pulsed signals, the capacitance of the LAAPD becomes dependent on the applied voltage, which in turn has an effect on the gain of the LAAPD. This behaviour has already been described by Oliver Noll in his collaboration talk[8]. This has to be taken into consideration when making assumptions about the gain, using an LED-pulser. Ths should also be taken into consideration for the final detector, since the signals are not continuous as well. An in-situ characterization as described in [8] was attempted, but could not be finished due to time constrains.

For this reason, the optimal energy resolution has been measured with the applied bias voltage as optimized parameter instead of the gain.

The optimal energy resolution has been found at a voltage of $359\,\mathrm{V}$, which corresponds to a gain of approximately M = 500 using the inaccurate characterization measured for continuous illumination.

With the limited dynamic range of the utilized APFE ASICs, only energies up to roughly $2.1\,\mathrm{GeV}$ can be measured with the proposed setting. This energy corresponds to an angular range in the laboratory system of angles larger 22° to 40°, depending on the beam current, out of the total range covered by the calorimeter of 22° to 140°. This means in terms of energy resolution, the LAAPDs should not be operated with a homogenous gain, but should be adjusted according to their position.

In order to verify the gain, an characterization with pulsed signals is planned, as well as a test of the measured optimal setting in a future beamtime.

A test of the settings for a crystal with two LAAPDS, as well as a damaged crystal, in order to see if there is a change in bevahiour of the optimal gain with radiation damage is recommended.

Contents

1 Introduction

1.1 Motivation

Ever since physics was established as a scientific discipline, physicists have been interested in learning about the fundamental laws and interactions that govern the state of matter and the universe itself. Gradually, scientists were able to describe forces on an ever smaller scale and tried to find fundamental particles.

In order to understand interactions and to verify or refute theories, complex and precise measuring equipment is necessary. Especially in the field of subatomic physics most experiments are quite complex and costly, therefore such projects are usually built within international collaborations.

One of the many tasks to fulfill, before a detector can be put to use, is to make sure each and every individual part of it works to its highest capacity and effciency.

For the electromagnetic calorimeter one of the many demands is an excellent energy resolution. Therefore the used photosensors in the given case, so called LAAPDs[1], have to be operated at their optimum performance. Because the signal to noise ratio and the excess noise are largely dependent on the gain, it is necessary to find the optimum gain working point for the maximum energy resolution. Since the readout electronics add to the electric noise, the gain optimum has to be tested, which is the object of this thesis.

---

[1]**L**arge **A**rea **A**valanche **P**hoto**d**iodes
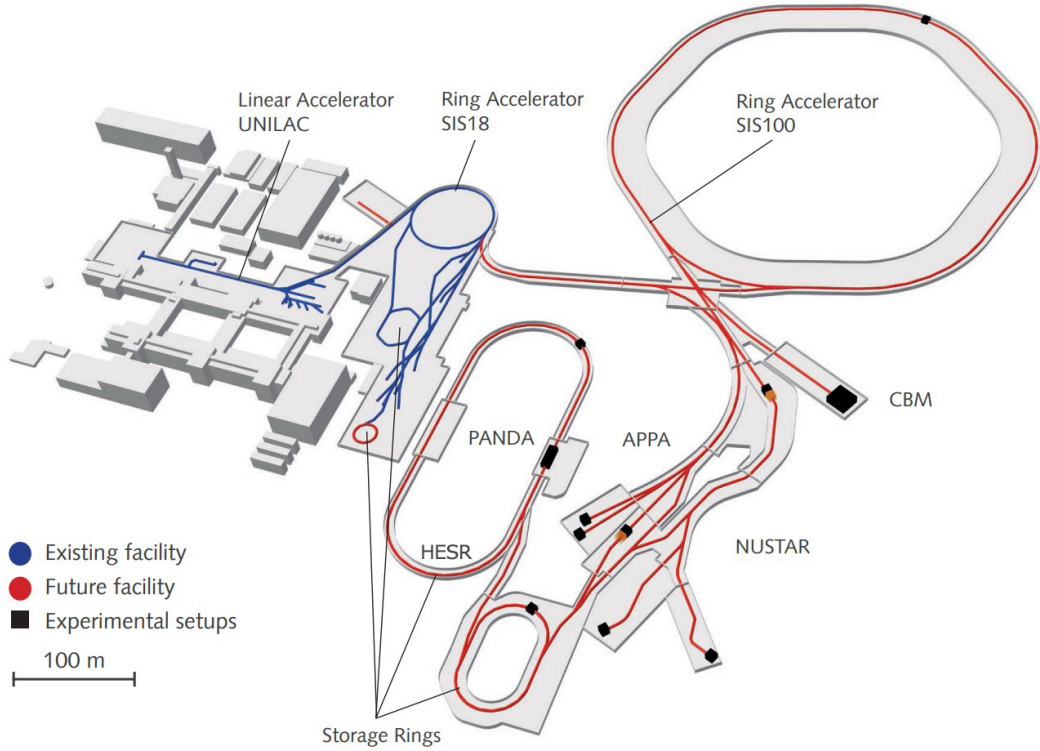
1.2 P̄ANDA at FAIR

Figure 1: Schematic of the future FAIR-facility[18].

FAIR[2] is an accelerator facility, which is currently under construction at the GSI Helmholtzzentrum für Schwerionenforschung in Darmstadt. It is supposed to extend the current facilities, which consist of a linear accelerator UNILAC[3] and a ring accelerator SIS18.

In addition to a new accelerator (SIS100) and three new storage rings (e.g. the CR and the HESR[4]), it will host a new class of several high-precision experiments. The goal of these experiments is to find new insights into the fundamental composition of matter, as well as answering questions about the evolution of the universe, in particular early stages after the big bang.

FAIR will cover a wide array of subjects, amongst which are atomic and plasma physics and their application (APPA), nuclear matter physics, in particular compressed baryonic matter (CBM), nuclear structure and astrophysics (NUSTAR) and experiments with high-energy antiprotons (P̄ANDA).

---

[2]**F**acility for **A**ntiproton and **I**on **R**esearch
[3]**UNI**versal **L**inear **AC**celerator
[4]**H**igh**E**nergy**S**torage**R**ing

The P̄ANDA[5]-experiment will use a cooled antiproton beam with momenta up to 15 $\frac{\text{GeV}}{\text{c}}$ from the HESR, which will collide with a fixed proton target made up of liquid hydrogen or a dense target of heavy nuclei.

It will try to answer questions about the strong interaction between hadrons and their composition in the context of quantum chromodynamics, especially the following topics:

- Hadron spectroscopy, in particular the search for exotic particles and their properties, as well as charmonium spectroscopy, D-meson spectroscopy, baryon spectroscopy and gluonic excitations

- The composition of the nucleon, of special interest are generalized parton distributions and and the time-like formfactor of protons

- Interactions of hadrons with matter (understanding the mass of hadrons and their role in spontaneous chiral symmetry breaking in QCD)

- Hypernuclei

Due to the short decay time of the produced states, the decay products will be measured and properties such as mass, momentum and quantum numbers will be analyzed. In order to reconstruct these states, the detector has to meet a wide array of requirements with regard to e.g. solid angle coverage, particle identification, luminosity and energy resolution.
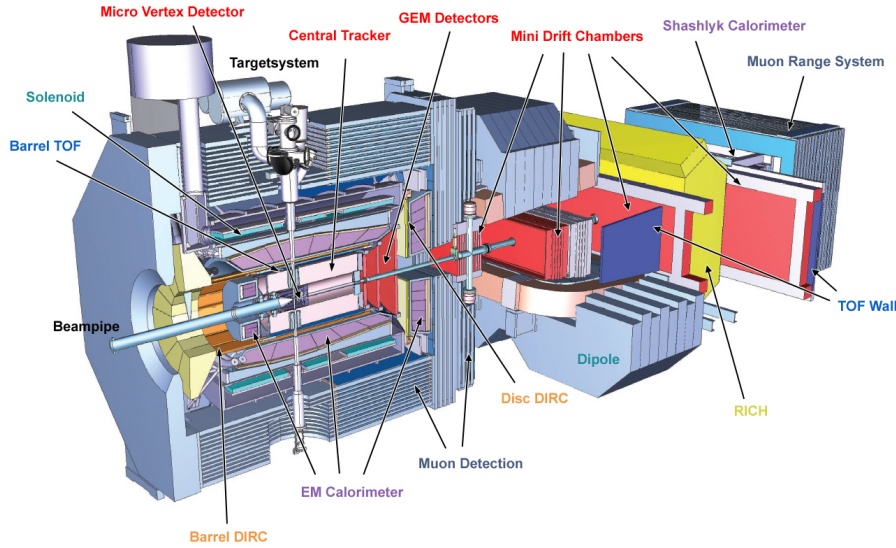
Figure 2: The P̄ANDA-detector[3].

As shown in figure 2, the P̄ANDA-Detector will consist of two main parts, the target spectrometer (TS) around the interaction point and the forward spectrometer (FS), which will analyze the forward going particles. Of particular interest in this thesis will be the target spectrometer.

The innermost part of the detector consists of the micro vertex detector around the beamline. It can detect the trajectories of charged particles, with a focus on secondary decay vertices of short lived particles. The MVD will be surrounded by the straw tube tracker,

---

[5]Anti**P**rotonen**A**nnihilation in **DA**rmstadt

which is based upon single channel drift tubes and also measures trajectories of particles with a longer lifetime. The next layer will be the DIRC-detectors followed by a time-of-flight system and the electromagnetic target calorimeter(EMC). The EMC will measure the energy loss of impinging particles as well as their position. The 2 T magnetic field in the target spectrometer will be provided by a solenoid magnet.

In addition, the target spectrometer will also have a myon detector system embedded in the magnet return yoke.

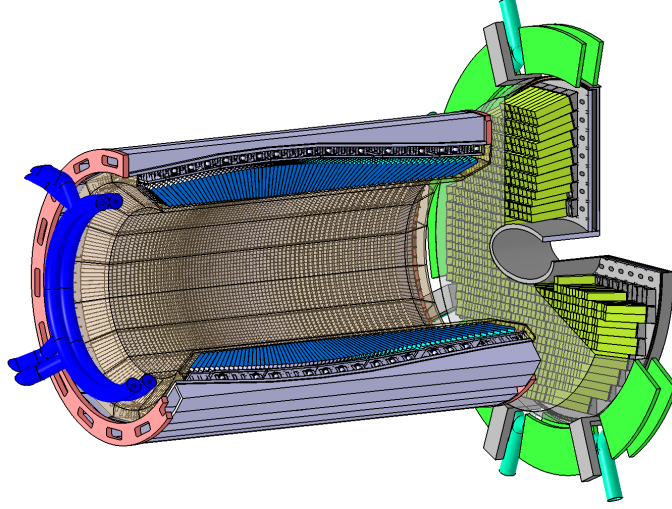### 1.2.1 The Electromagnetic Target Calorimeter

Figure 3: Schematic view of the electromagnetic calorimeter without the backward endcap.

The electromagnetic calorimeter is one of the key components of the $\bar{\mathrm{P}}$ANDA experiment. Its most important function will be measuring the deposited energy of high-energy particles and their direction via determining the point of impact. In order to guarantee a precise measurement a coverage of almost the complete solid angle, as well as a precise energy measurement over the full energy range, is required.

The EMC will consist of three separate parts: the barrel electromagnetic calorimeter, the forward endcap (FEC) and the backward endcap (BEC).

In total there will be 15552 $PbWO_4$ crystals installed in the EMC, with 11360 in the barrel, 3864 in the FEC and 592 in the BEC[1]. Each crystal will be read out by two Large Area Avalanche Photodiodes supplied by Hamamatsu1.2.3, except the inner most part of the forward endcap, which wil be read out by Hamamatsu vacuum phototetrodes[19].

The barrel willcomprise 16 slices with 710 crystals each. In order to reach the wanted barrel shape and minimize the empty spaces between crystals, there will be 11 different geometries, including a mirrored version for each type. The overall requirements for the EMC are as follows:

Properties	Design value
energy resolution $\frac{\sigma(E)}{E}$	$\frac{<2\%}{\sqrt{E/\text{GeV}}} \oplus \leq 1\%$
energy threshold	$\leq 10\,\text{MeV}$
individual crystal threshold	$\leq 3\,\text{MeV}$
noise equivalent $\sigma_{E,noise}$	$\leq 1\,\text{MeV}$
solid angle coverage $\frac{4\pi}{\%}$	$99\,\%$
Subunit properties	Barrel EMC ($140\,° \geq \Theta \geq 22\,°$)
dynamic range	$7.3\,\text{GeV}$
position resolution σ_θ	$0.3\,°$
maximum signal rate	$100\,\text{kHz}$
shaping time	$400\,\text{ns}$ (LAAPD)
radiation hardness (annual dose)	$10\,\text{Gy}$

Table 1: Overview of main requirements for the P̄ANDA-EMC[12].

1.2.2 Scintillation and Calorimetry

In general, the determination of the total energy of high energy particles is called calorimetry. A calorimeter measures the deposited energy of an impinging particle via scintillation light.

In order to understand how a calorimter is built and which characteristics are of interest, the fundamental processes of the energy-loss of particles in matter have to be understood. Generally, these interactions can be sorted into two different categories:

- **Interaction of charged particles with matter**
  When particles pass through matter, they usually change their direction as well as their energy due to their interactions with the atoms. Those interactions are[22]:

  - Ionization and excitation of atoms through
  - Elastic and inelastic scattering
  - Bremsstrahlung (emission of photons by decelerated electrons and positrons in the electric field of a nucleus)
  - Cherenkov- and transition radiation

Since transition radiation and Cherenkov radiation are only responsible for a small amount of energy loss, they can be neglected for heavy or highly ionized particles. For such particles, usually ionization dominates the energy loss, while the energy loss of light particles, such as electrons and positrons, is usually dominated by bremsstrahlung. The mean energy loss of particles in matter can be described by the Bethe-Bloch-formula [20]:

$$\left\langle -\frac{\partial E}{\partial x} \right\rangle = K z^2 \frac{Z}{A} \frac{1}{\beta^2} \left[\frac{1}{2} \ln \frac{2 m_e c^2 \beta^2 \gamma^2 W_{max}}{I^2} - \beta^2 - \frac{\delta(\beta\gamma)}{2} \right]. \tag{1}$$

As seen, the energy-loss is mostly dependent on the atomic charge Z and the velocity β of the particle. In order to identify particles, one can plot the energy loss against their momentum (see figure 4).
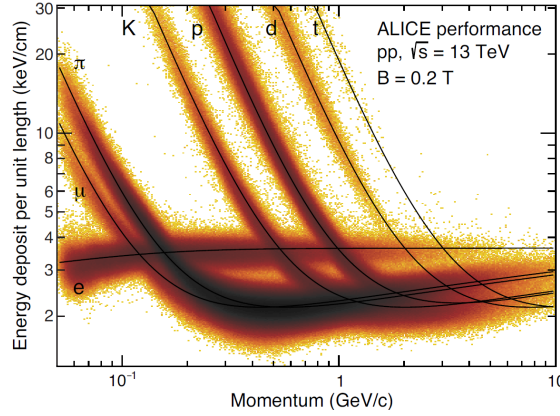
Figure 4: Energy loss for different particles plotted against their momenta[23].

- **Interaction of photons with matter**
  The dominant processes for photons are the photoeffect (the photon transfers its whole energy onto an atom, which emits an electron), the Compton effect (elastic scattering of the photon on an orbital electron) and pair production (the photon converts into an electron-positron pair), depending on the photon energy.
  The intensity loss of the radiation can be described by the following equation[22]:

$$I(x) = I_0 \cdot e^{-\mu x} \tag{2}$$

  with I_0 being the starting intensity, x the thickness of the material (or rather, the length traversed by the photon) and μ the mass absorption coefficient. μ can be described by[22]

$$\mu = N_a \cdot \frac{\rho}{A} \cdot \sigma \tag{3}$$

$$\sigma = \underbrace{\sigma_{ph}}_{\text{Photoeffect}} + \underbrace{\sigma_C \cdot Z}_{\text{Comptoneffect}} + \underbrace{\sigma_P \cdot}_{\text{Pairproduction}} \tag{4}$$

  With N_a being the Avogadro-constant, ρ the density of the material, A the geometrical cross-section and σ the interaction cross-section. Detailed equations for the cross sections can be found in[22].

A high-energy particle will usually produce a particle shower. Depending on the shower type, the detecting calorimeters can be divided into two groups: electromagnetic calorimeters, which primarily measure electrons, positrons and photons and hadronic calorimeters. Electromagnetic showers occur when a charged high-energy particle traverses dense matter and emitts photons or when a high-energy photon does pair production. The resulting particles/photons can then emit photons or do pair production themselves, which results in a cascade of secondary particles.

In order to describe the evolution of such a shower, "Approximation B" by Rossi is often used[24]. His main assumptions are:

- The shower will be mostly comprised of electrons, positrons and photons. Since bremsstrahlung and pair production dominate for these particles, only their contributions will be taken into account.

- The energy loss through ionization is equal to the critical energy per radiation length.

- The shower distribution will be only discussed in one dimension and multiple scattering will be neglected.

By applying these restrictions, the characteristics of an electromagnetic shower can be estimated. One of these properties is the radiation length X_0.
For photons, it is proportional to the mean free path length:

$$l \approx \frac{9}{7} X_0 \tag{5}$$

For electrons it determines the relative energy loss per path length:

$$\frac{dE}{E}|_{ion}(E_c) \approx \frac{E_c}{X_0} \tag{6}$$

Electrons and photons will mostly lose their energy via bremsstrahlung and pair production until they reach a critical energy E_c. Below this energy threshold, the leftover electrons will mostly interact through ionisation. If this model is used, one can assume, that the deposited energy inside the material E_0 is proportional to the total number of produced particles:

$$N_{tot} \approx \frac{E_0}{E_c} \tag{7}$$

$$s_{tot} \approx \frac{E_0}{E_c} \cdot X_0 \tag{8}$$

Moreover, it is also plausible to assume that after a radiation length one of the two processes will happen and that the produced particles should have in average half of the energy of the former particle. This means, after a distance of $s = n \cdot X_0$, the total number of particles and the energy of each particle is given by:

$$N = 2^n \qquad\qquad E = \frac{E_0}{2^n} \tag{9}$$

Therefore, the depth of the shower is $s_{max} = n_{max} \cdot X_0$ which can be calculated by using the critical energy:

$$E = E_c = \frac{E_0}{2^{n_{max}}} \tag{10}$$

E_c can also be used to calculate the maximal number of particles produced:

$$N_{max} = \frac{E_0}{E_c} \qquad\qquad n_{max} = \frac{\ln(\frac{E_0}{E_c})}{\ln(2)} \tag{11}$$

As described by these equations, the number of particles grows linear with the energy of the original particle, while n_{max} only grows logarithmically with the energy of the original particle.
The expansion of the shower plays a big role in the geometric dimensions of the calorimeter. Therefore the **lateral shower profile** has to be taken into consideration: With the two dominant shower processes mentioned before, the particles usually scatter for high energies under small angles, which are proportional to $1/\gamma$.
The lateral distribution is dominated by multiple scattering of low energy particles, as well as compton-scattering for the photons. A measure for this distribution is the so called

"Moliére-radius", which describes the radius of a cylinder around the shower axis, in which 90% of the energy of the original particle is deposited:

$$R_M = \frac{21.2\,\text{MeV}}{E_c} \cdot X_0 \tag{12}$$

Therefore, the granularity of the detector material should be of the same scale or smaller than R_M for a good position reconstruction. Since the longitudinal distribution of the shower scales with the radiation length, the shape of the shower is described by the ratio of the Moliére-radius and the radiation length:

$$\frac{R_M}{X_0} \propto \frac{1}{E_c} \propto Z \tag{13}$$

with Z being the atomic number of the detector material, which means a shower in aluminum will be slimmer than one in lead. All these characteristics have to be considered when building a calorimeter.

As mentioned in ch. 1.2.1, an electromagnetic calorimeter will use scintillation as a form of energy measurement.
Scintillation is a process, in which ionizing radiation can be detected by measuring light that occurs in particular materials (scintillators) due to energy absorption.
For a detector with a sufficient resolution and a high efficiency, there are a few requirements for the scintillator[21]:

- A high light yield for an adequate signal

- Transparency for the wavelength of the emitted scintillation light

- Very short light pulses with no or little emission delay

- Proportionelity between the energy loss of a particle and the amount of emitted light

Organic as well as inorganic materials show scintillation properties. Inorganic scintillators are mostly composed of ionic crystals, which usually contain a large fraction of atoms with high-Z nuclei, which leads to a short radiation length.
In these materials, the process is dependent on the properties of the electronic band structure: to scintillate, a crystal needs so-called luminescence centres, whose energy levels are lower than the bandwidth between the valence band and the conduction band and which have transitions in the visible or near visible wavelength region. Such centres can either be intrinsic, e.g. ions or strucural defects, or can be induced by doping the material with an appropriate substance.
When an ionizing particle or a photon with sufficient energy passes through a scintillator, it will generate free charge carriers. If these travel to the nearest luminescence center, they can excite the center and it will deexcite through emission of a photon.
The emitted light can be reabsorbed within the material. To prevent self-absorption, luminsecnece centres open for the Stokes-Shift effect, which is shift of the wavelength between absorption and emission, are needed.
Therefore, an ideal scintillator should have low self-absorption in order to generate a high light yield, which means the wavelength area of emission and absorption should overlap as little as possible.

1.2.2.1 PWO-II as Scintillation Material The P̄ANDA EMC has specific requirements for the utilized scintillation material[12]:

- High rate capability, which requires fast scintillation kinetics

- Appropriate granularity to minimize pile-up as well as guarantee optimum position reconstruction of the center of the electromagnetic shower

- Sufficient luminescence yield to achieve good energy resolution in particular for the lowest photons in the MeV range, which goes in parallel with a minimum energy threshold of the individual crystal

- Timing information, primarily to reduce background and to provide an efficient correlation with other detector components for particle identification

- Adapted geometrical dimensions to contain the major part of the electromagnetic shower and to minimize the impact of leakage fluctuations

- Radiation hardness to limit the loss in optical transparency and therefore light output to a tolerable level

- Sufficient compactness, since the size of the EMC is directly limited by the solenoid magnet

The requirements are fulfilled by PWO-II, an improved $PbWO_4$ scintillator. Due to its short radiation length X_0 and small Moliére radius R_M, caused by the high-Z materials, it enables a compact design of the calorimeter. Furthermore, the material has a relatively short decay time of $6.4\,\text{ns}$, with $80\,\%$ of the scintillation light being collectable within $20\,\text{ns}$ at room temperature[4]. Unfortunately, lead tungstate has a low light yield compared to other scintillators. In order to guarantee a sufficent light yield, the crystals will be cooled to -25 °C which increases the light yield by factor of about 4 compared to room temperature. In addition, each crystal will be wrapped in reflective foil in order to optimize light output. Even though the scintillation kinetics become slower with lower temperatures, it is still possible to collect $97\,\%$ of the light within a time gate of $100\,\text{ns}$[4]. This makes the material capable of the desired high count rates.

Parameter	PWO-II
ρ [g/cm^3]	8.28
X_0 [cm]	0.89
R_M [cm]	2.00
τ_{decay} [ns]	6.5
λ_{max} [nm]	429
index fo refraction at λ_{max}	2.17
relative Light Yield compared to NaI	2.5 at -25 °C
hygroscopic	no
$\frac{dLY}{dT}$ $\left[\frac{\%}{°C}\right]$	-3.0 at Room Temperature
$\frac{dE}{dx}$(MIP)$[\frac{\text{MeV}}{\text{cm}}$	10.2

Table 2: Relevant properties of $PbWO_4$[12]

As mentioned in section 1.2.1 there will be 11 different crystal geometries in order to obtain the barrel shape while mounting, with two mirrored versions for each type. Each crystal wil be $20\,\text{cm}$ in length.
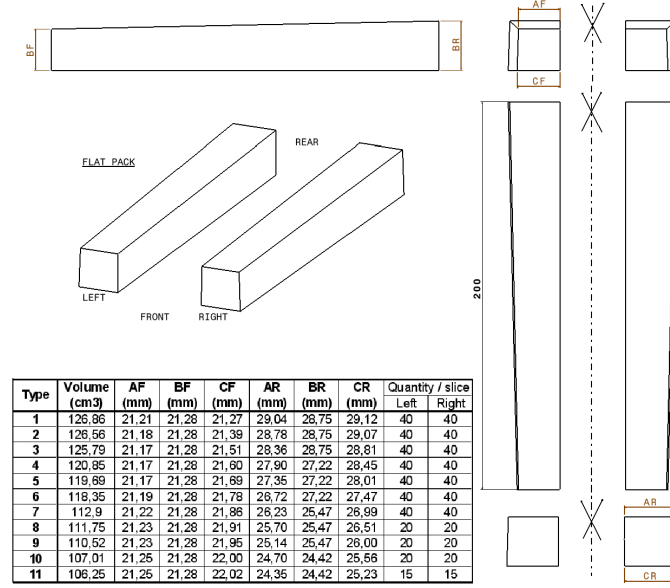
Type	Volume (cm3)	AF (mm)	BF (mm)	CF (mm)	AR (mm)	BR (mm)	CR (mm)	Quantity / slice	
								Left	Right
1	126,86	21,21	21,28	21,27	29,04	28,75	29,12	40	40
2	126,56	21,18	21,28	21,39	28,78	28,75	29,07	40	40
3	125,79	21,17	21,28	21,51	28,36	28,75	28,81	40	40
4	120,85	21,17	21,28	21,60	27,90	27,22	28,45	40	40
5	119,69	21,17	21,28	21,69	27,35	27,22	28,01	40	40
6	118,35	21,19	21,28	21,78	26,72	27,22	27,47	40	40
7	112,9	21,22	21,28	21,86	26,23	25,47	26,99	40	40
8	111,75	21,23	21,28	21,91	25,70	25,47	26,51	20	20
9	110,52	21,23	21,28	21,95	25,14	25,47	26,00	20	20
10	107,01	21,25	21,28	22,00	24,70	24,42	25,56	20	20
11	106,25	21,25	21,28	22,02	24,35	24,42	25,23	15	15

Figure 5: Geometry of the different crystals[3].

The crystals will be fixed in their position by a thin carbon alveole with glued plastic front stoppers and a metal insert at the rear, which will later be mounted onto the back plane construction of the corresponding slice.

1.2.3 LAAPD

The readout electronics for the electromagnetic target calorimeter need to be radiation tolerant, have a high quantum effciency at the maximum emission wavelength of lead tungstate, be insensitive to high magnetic fields (therefore photomultipliers cannot be used as readout electronics, since the photodetectors need an intrinsic amplification), and be low cost in mass production[12].

In order to meet these criteria, large area avalanche silicon photodiodes have been developed in cooperation with Hamamatsu. These LAAPDs are reverse biased diodes, which use an internal electric field in order to multiply charge carriers via the avalanche effect.

The LAAPDs are made out of a layer of Si_3N_4 as a passivation layer in order to decrease the losses from reflection on their surface, a highly doped p^{++}-layer, a lower doped pn-junction and two highly doped n^{++}-layers, with the highly doped layers acting as electrodes (see fig.6).
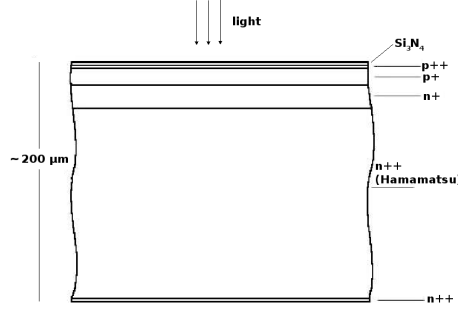
Figure 6: Schematic structure of a LAAPD[12]

When light enters the LAAPD via the silicone layer and is absorbed by the p$^+$-layer, electron-hole pairs are created.

While the electrons drift towards the n$^+$-side, the positive holes drift towards the p$^+$-side. Due to the high voltage on the p^{++} and the n^{++}-layers, an electric field of approximately $10^7 \frac{V}{m}$ is created in the contact area. The free charge carriers are accelerated and generate new pairs, which are also accelerated within the electric field and are able to generate more pairs, which leads to an avalanche effect that multiplies the original signal significantly.

This internal amplification in relation to the voltage between the highly-doped layers is measured for the individual LAAPDs at sites of partner groups involed in the $\bar{P}$ANDA-EMC. The dark current I_d and the current under continous illumination I_{ill} at the maximum emission wavelength of $\lambda = 420\,$nm is measured for several bias voltages up to breakdown. The gain is then defined as the ratio between the difference of the currents for the set bias voltage and the difference in currents for a bias voltage where amplification not yet occurs[12]:

$$M = \frac{\mathrm{I}_{ill}(U) - \mathrm{I}_d(U)}{\mathrm{I}_{ill}(\mathrm{M}=1) - \mathrm{I}_d(\mathrm{M}=1)} \tag{14}$$

The gain also depends on the temperature, as seen in fig. 68. In order to ensure a precise measurement, both parameters have to be stable and within a range of $\Delta T = \pm 0.1°$C and $\Delta U = \pm\ 0.1$V[12].

The amplified signal is proportional to the intensity of the scintillation light and can be used as a measurement for the energy loss of a particle passing the crystal.

The active area of the LAAPDs has to be quite large to obtain a good energy resolution down to 10 MeV. For suppressing nuclear counter effects and for resolution purposes, there will be two rectangular APDs used per crystal.

They have a thickness of roughly $200\,\mu$m and a surface area of $9.0 \times 18.0\,$mm^2, with an active area of $6.8 \times 14\,$mm^2.
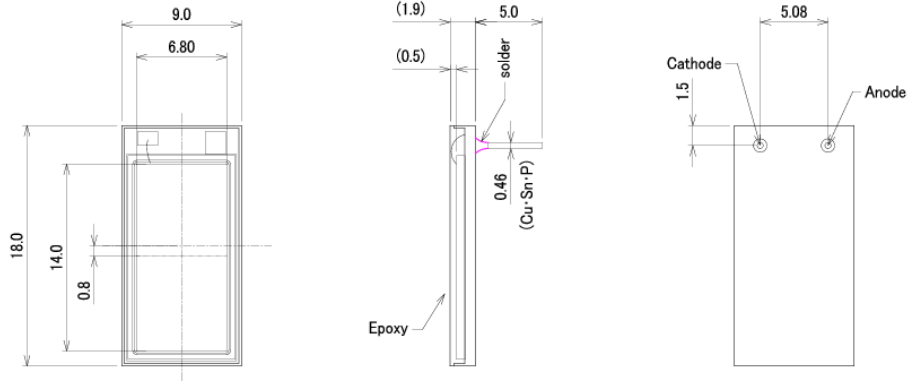
Figure 7: Technical drawing of the LAAPDs[12].

Since the charge carrier multiplication within the LAAPD is a statistical process, it contains fluctuations. Even though the gain stays constant as long as the voltage stays constant, there is still an excess noise from the non-uniformity of individual carrier ionization.

This excess noise adds to the shot noise of the APD, which can be calculated by the following equation[13]:

$$In^2 = 2q(I_L + I_{dg})BM^2F + 2qI_{ds}B. \tag{15}$$

With q being the electron charge, I_L the photocurrent at gain = 1, I_{dg} and I_{ds} refer to the dark current (see below), B ist the bandwidth, M the gain, and F refers to the excess noise factor.

The dark current of the APD can be split up in two parts: One component of the dark current is the surface leakage current (I_{ds}) between the PN junction and the silicon oxide layer. The other component is the internal dark current (I_{dg}) generated in the Si subrate. This leads to the following equation[13]:

$$I_D = I_{dg} + M \cdot I_{ds}. \tag{16}$$

Furthermore the excess noise factor F can be expressed by[13]

$$F = Mk + (2 - \frac{1}{M})(1 - k), \tag{17}$$

with k being the ratio of the electron/hole ionization rate. As seen in this equation, the excess noise will increase with increased gain. The signal to noise ratio of the LAAPDs can be calculated by

$$\frac{S}{N} = \frac{I_L^2 M^2}{\underbrace{2q(I_L + I_{dg})BM^2F + 2qI_{ds}}_{shotnoise} + \underbrace{\frac{4kTB}{R_L}}_{thermalnoise}} \tag{18}$$

with k being Boltzmanns constant, T the absolute temperature, and R_L the load resistance. The optimum gain where the signal-to-noise ratio is maximized, if I_{ds} can be ignored, can be described by[13]

$$M_{opt} = \left[\frac{4kT}{q(I_L + I_{dg}) \cdot x \cdot R_L}\right]^{\frac{1}{2+x}} \tag{19}$$

where x describes the excess noise index $(F = M^x)$, see [13]. A visual representation of the afore mentioned process can be seen in fig. 8.

Famp: Noise figure of next-stage amplifier
Rin : Input resistance of next-stage amplifier
k   : Boltzmann's constant
T   : Absolute temperature
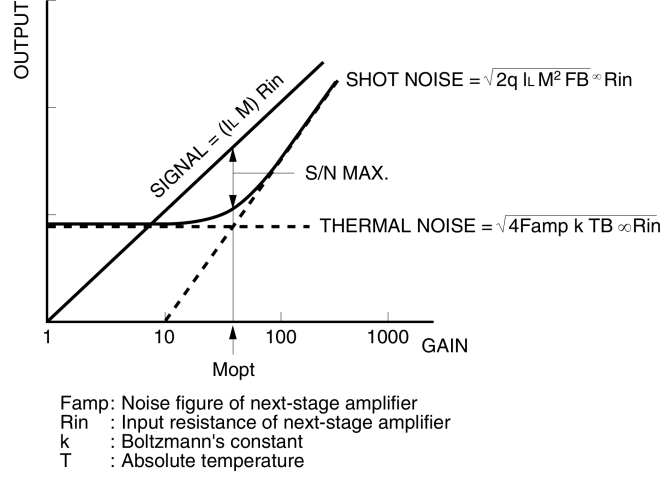
Figure 8: APD gain vs output with an indication of how to maximize S/N[13].

The energy resolution of the LAAPDs can be described by[3]

$$\frac{\sigma_E}{E} = \sqrt{\frac{F}{N_{eh}}} \tag{20}$$

with F being the excess noise factor and N_{eh} the number of electron-hole-pairs created within the LAAPD. As mentioned before, the excess noise factor increases with the gain, but the numbers of electron-hole pairs as well. Since N_{eh} can also be described as LY (light yield)$\cdot E$, the formular can be written as

$$\frac{\sigma_E}{E} = \sqrt{\frac{F}{LY \cdot E}} \tag{21}$$

Moreover, the energy calibration can be parametrized as[3]:

$$\frac{\sigma(E)}{E} = \sqrt{\underbrace{(\frac{a}{\sqrt{E}})^2}_{A} + \underbrace{(\frac{b}{E})^2}_{B} + c^2,} \tag{22}$$

Where A is affected by the excess noise factor and the photonstatistics, B is affected by the electronic noise and the constant term describes inhomogeneities and inaccuracies.

1.2.4 APFEL-ASIC

The readout electronics for the barrel EMC need to be fast, have a low noise level and low power consumption.
In order to meet these criteria the APFEL[6] preamplifier was developed. It converts the charge signal generated by the LAAPD into a voltage pulse, which is then digitized by a sampling analog-to-digital converter (SADC).

---

[6]**A**SIC for **P**ANDA **F**ront-end **EL**ectronics

The APFEL has two channels per chip. Each consists of a charge sensitive preamplifier, a third order semi-Gaussian shaper stage and a differential output driver.

The input of the ASIC for one LAAPD is split into two outputs with different programmable amplifications. One output, the so called "low gain" is operated at an amplification of 1, while the other output, the so called "high gain", can be set to an amplification of either 16 or 32. This design enables the detector to be sensitive to low energies, while still covering the full dynamic range.

Its maximum input charge is $8.5\,\mathrm{pC}$[11] resulting in a dynamic range of over 10000.

Since the APFEL will be within the cold volume of the barrel EMC, it needs to be low in power consumption. With a consumption of less than $120\,\mathrm{mW}$ per ASIC[11], this condition is met. Moreover, the APFEL is able to handle the foreseen event rate of $350\,\mathrm{kHz}$.

Additional features are an optional charge injection, which can be used as a test pulser, the possibility of writing and reading the DAC registers for signal-baseline adjustments as well as an auto calibration feature. Each APFEL has an ID for single chip and Bus communication.[12][1]

Schematics of the APFEL preamplifier can be seen in fig. 9. Each channel corresponds to one APD on the crystal.
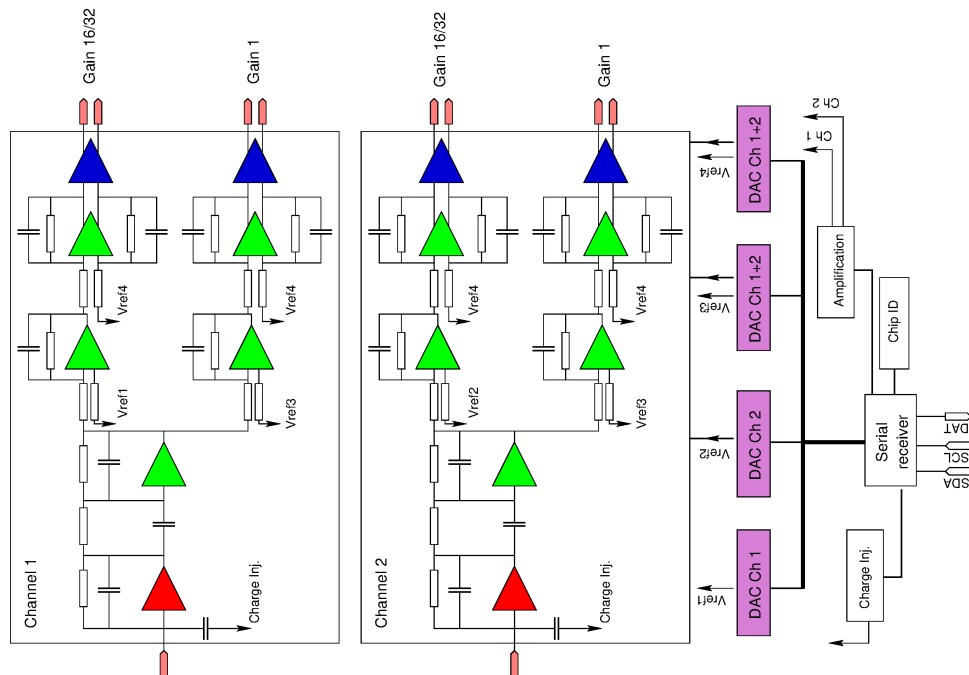
Figure 9: Schematic layout of the APFEL, where red shows the charge sensitive preamplifier, green the third order shaper stage and blue the differential output driver.

2 Setup

In order to obtain relevant results for the $\bar{\mathrm{P}}$ADNA experiment, the utilized setup and conditions should be as close as possible to the final setup. For this reason, measurements were conducted inside a programmable climate chamber from Weiss Umwelttechnik GmbH and close to final $\bar{\mathrm{P}}$ANDA readout equipment was used.
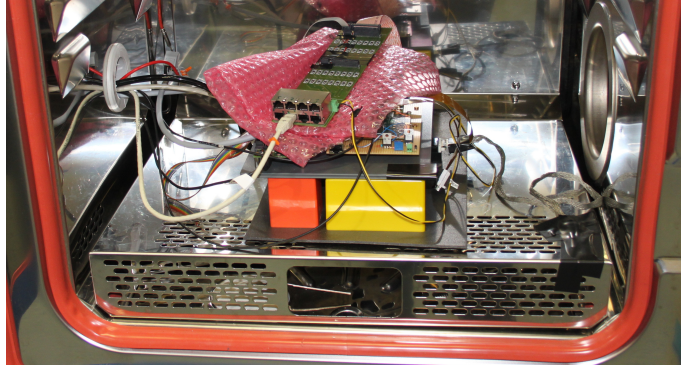
Figure 10: Crystal with readout electronics inside the climate chamber.

A PbWO$_4$ crystal of type 6 geometry was used as a scintillator, with a single rectangular LAAPD (serial number: 0911009793) serving as a photodetector. The LAAPD is coupled to the crystal with silicon oil[7] and is additionally held in place with a plastic casing and black tape.

In order to minimize light loss, the crystal is wrapped in reflective material as well as opaque tape.

As a reference signal, a $\bar{\mathrm{P}}$ANDA LED-pulser prototype from the Bochum $\bar{\mathrm{P}}$ANDA group was used, which is supposed to mimic the pulse shape of PWO-II scintillation, after the ASIC. It can be used to simulate the scintillation of lead tungstate for energies up to 15 GeV[6]. The pulser is controlled via a RaspberryPi interface, where frequency, transmittance of the optical attenuator (and therefore the intensity of the light pulses) can be regulated. Moreover, three LEDs are built into the pulser, with different wavelength regions (red, green and blue). For emulating lead tungstane crystals, the blue one with a wavelength between 440 nm and 460 nm was used for all measurements. The user interface can be seen in fig. 11
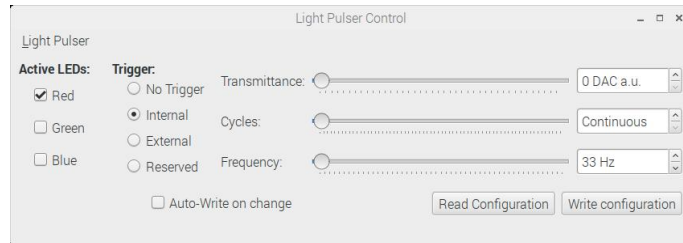
Figure 11: User interface of the LED-Pulser, courtesy by[17].

While it is possible to adjust the transmittance of the optical attenuator in arbitrary units, the intensity of the pulser shows no linear behaviour towards the transmittance. A lower

---

[7]"Basilone" M 300000

setting will increase the intensity of the light pulse, while a higher setting will decrease it. Generally, the intensity does not change significantly when the transmittance value is lower than 500 DAC a.u. (see fig.70). In addition, the pulser does not possess an intrinsic stabilization. It is therefore not trivial to reproduce intensities, when the pulser has been turned off.
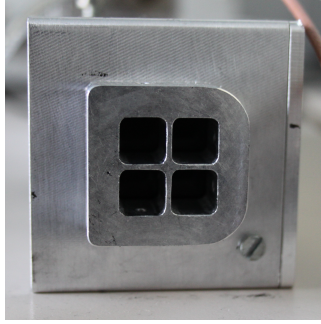
(a) Outlet of the pulser.
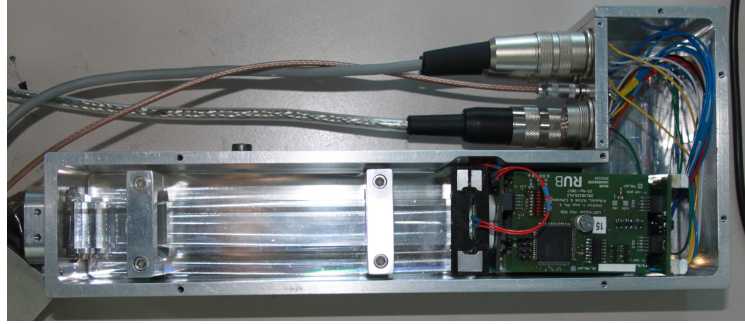
(b) Interior of the LED-pulser.

Figure 12: LED-pulser.

As seen in fig. 12, the pulser has an outlet with can hold up to four different bundles of fibers. For this setup raytela toray optical plastic fibers have been used. They are made from fluorinated polymer with a layer of polymethyl methacrylate and have a thicker diameter than the quartz fibers forseen for $\bar{\text{P}}$ANDA. They were cut to a suitable length and put into an opaque plastic tube. In order to mount them onto the pulser and the crstal, they were glued on both sides into black plastic bits, which fit the outlet of the pulser. Both sides have also been polished.

For the crystal, an iron flange was made with a hole similar to that of the pulser outlet, with plastic screws on top for fixing the fibers firmly in place. The flange has been taped onto the crystal with black foil. Both the flange and the plastic bit for the fibers can be seen in fig. 13.

(a) Optical light fibers in plastic bit.
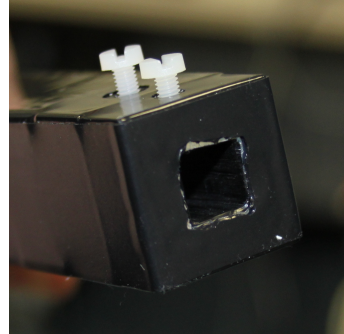
(b) Iron flange for the optical fibers on top of the crytsal.

Figure 13

To increase the light output further the fibers were additionally coupled to the pulser and the crystal with optical grease.

Figure 14: Wrapped crystal equiped with LAAPD and flange.

The LAAPD went through the full $\bar{\text{P}}$ANDA screening procedure, which includes annealing and characterization. The gain-voltage curve for continuous illumination (DC) has been measured at the PSL[8] of the GSI[9] in Darmstadt. The LAAPD is supplied with power via an ISEG crate with EHS F210p-F modules.
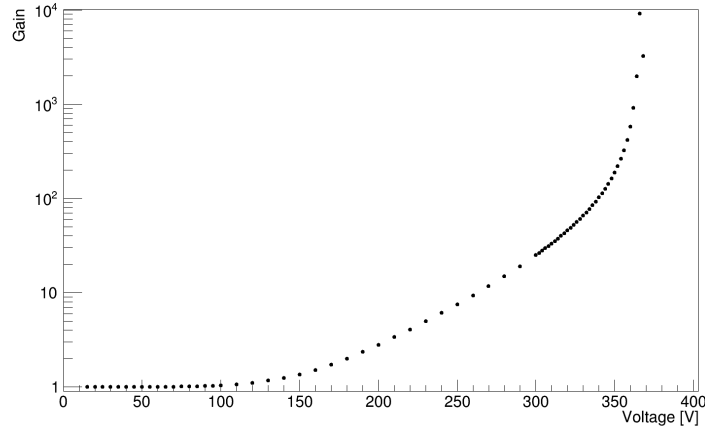
Figure 15: Gain characteristics of the utilized LAAPD under continuous illumination measured as described in ch.1.2.3 at a temperature of -25 °C.

The form of the curve can be described by the "Miller-function"[3]

$$M(U) = \frac{1}{1 - (\frac{U}{p_0})^{p_1}} + p_2. \tag{23}$$

With p_0 being the break down voltage. Since the gain characteristics differ from LAAPD to LAAPD, the Miller function does not always describe the behavior between gain and voltage perfectly over the whole voltage range. Therefore, the curve was split into smaller sections, which were fitted individually with the Miller function. From these the corresponding voltage was extrapolated. (Figure 16).

---

[8]PhotoSensorLab
[9]Gesellschaft für Schwerionenforschung

(a) gain 727 - 800   (b) gain 500 - 727   (c) gain 137 - 500

(d) gain 83 - 137   (e) gain 56 - 83   (f) gain 26 - 56

(g) gain 26 - 56
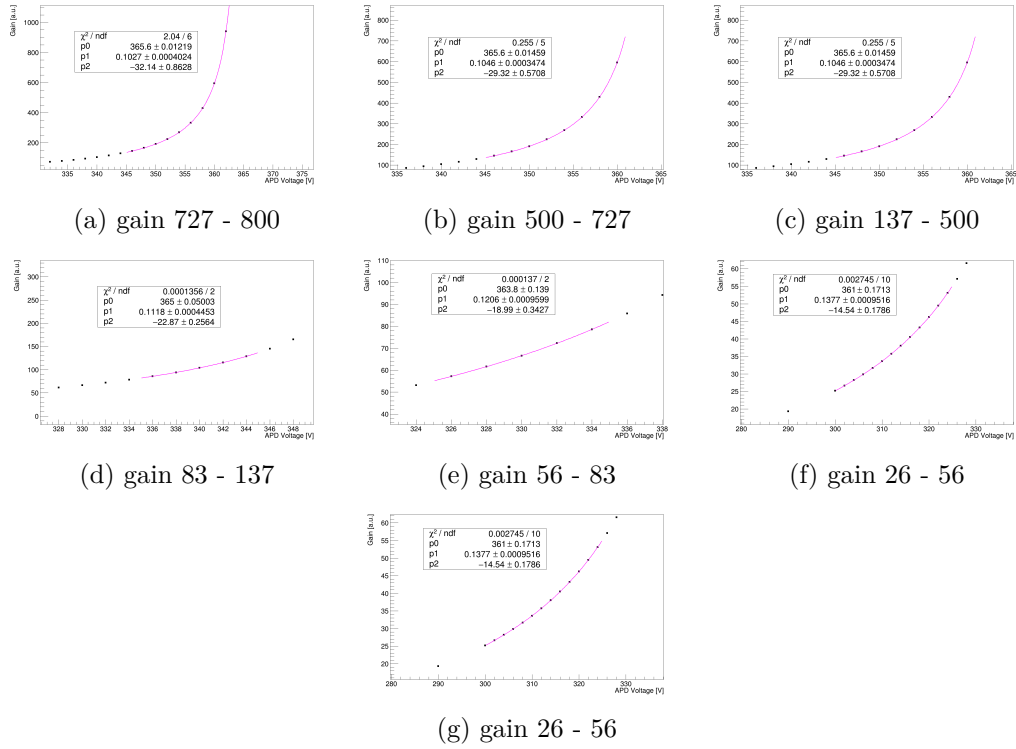
Figure 16: Fits for various gain ranges.
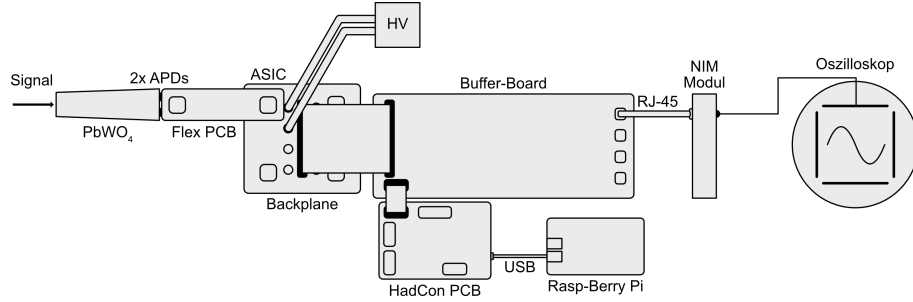
Figure 17: Schematic for the readout electronics inside the climate chamber, courtesy by[17]

Fig. 17 shows the schematics of the readout electronics inside the climate chamber. The LAAPD is directly connected to the APFEL, which is connected to the backplane via a Flex-PCB. Both the voltage supply for the APFEL as well as the high-voltage supply for the LAAPD is realized through the backplane.

(a) Bufferboard with connected signal cables.
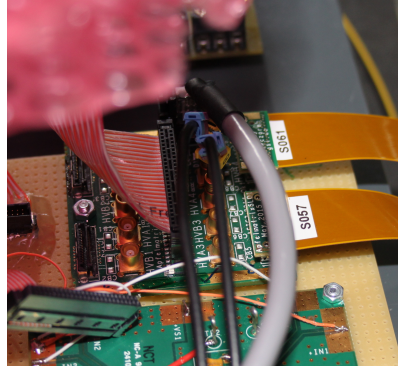
(b) Backplane with two mounted Flex-PCBs.

Figure 18

The backplane is connected to the bufferboard, which can forward the differential signals via networking cables to either an oscilloscope or a sampling analog-to-digital converter (SADC). Additionally, it has a connection to a HadConPCB, which is needed for controlling the DAC values of the APFEL. DAC settings, the programmable amplification of the high gain branch as well as a test pulser system are controlled through a CSS studio user interface. The backplane is operated at a constant voltage of 4 V and the bufferboard at 8 V.
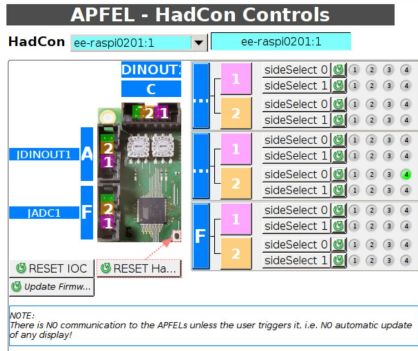
(a) HadCon controls. For the setup used, only connection C-2 with only one connected APFEL-ASIC is in use, indicated by the green dot. Courtesy by[17]
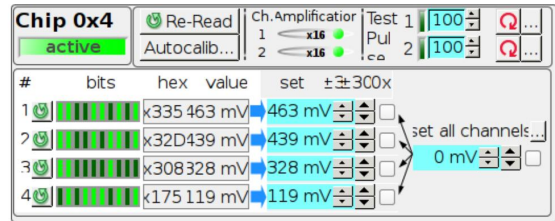
(b) Controls for a single APFEL. The amplification for the high gain and the baseline offset can be set here. Courtesy by[17]

Figure 19

When the APFEL ASIC is operated with the CSS studio interface, most settings are stable over long periods of time, excpect for the programmable channel amplification.

21
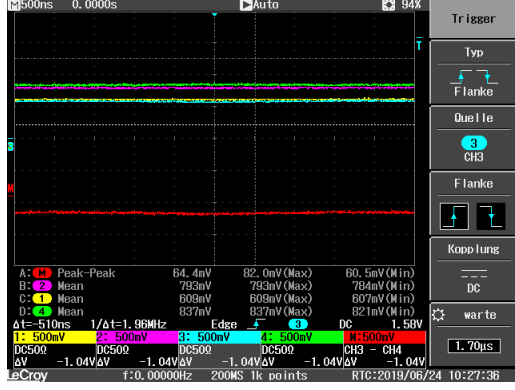
(a) Picture of the baselines for high gain and low gain taken with the oscilloscope before leavig the lab in the evening.
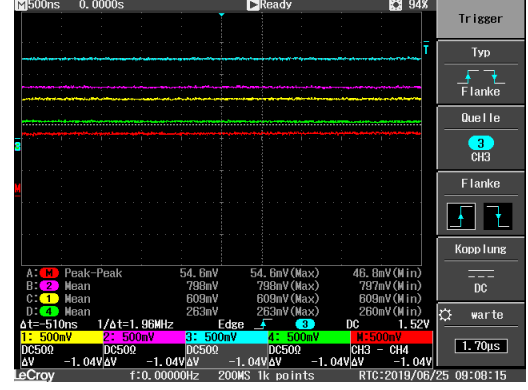
(b) Picture of the baselines for high gain and low gain taken with the oscilloscope the next morning after entering the lab.

Figure 20: Stability of the channel amplification.

As can be seen in fig. 20, the baselines for the high gain branch shift if the APFEL ASIC is not used. When the APFEL ASIC has been turned off, the amplification is no longer defined and the amplification has to be reinitialized. However, the amplification jumps to a default setting when the APFEL chip is idle for longer periods of time. This behaviour has been observed when the amplification is set to 16, as well as 32, though it is unclear if the problem arises from the CSS studio control programm or from the APFEL ASIC itself.
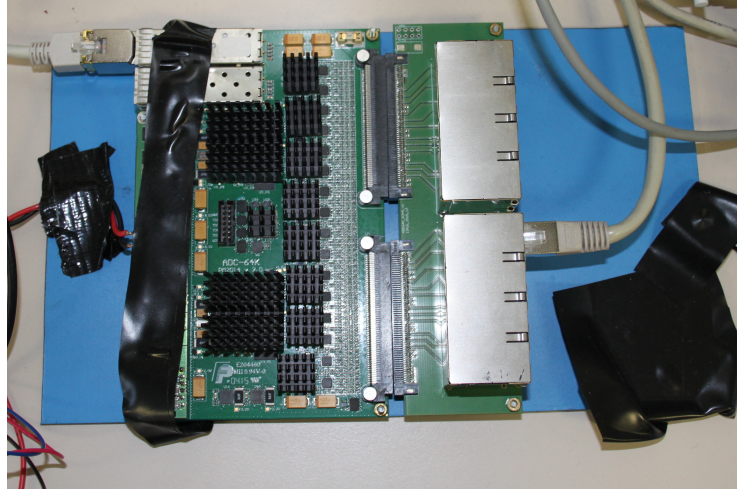
Figure 21: $\bar{P}$ANDA SADC designed by Pawel Marciniewskwi, Uppsala University.

As an analog-to-digital converter, a $\bar{P}$ANDA SADC designed by Pawel Marciniewskwi, Uppsala University, was used (see fig. 21).
Each input can read out four channels, which corresponds to two APDs with a high gain and a low gain channel each. The SADC can be accessed with two IP-adresses, one for each 32-channels. It has a sampling rate of 14bit @ 80 MHz, which translates to a time resolution of 12.5 ns, and an FPGA for onboard feature extraction, which was not used for this thesis. The SADC is operated using a python script programmed by Johannes Müllers.

22

3   Procedures

3.1   Energy Calibration of the LAAPD

In order to attribute the response of the setup to an energy, the equipment has to be calibrated. For this, cosmic muons were used since the most probable energy loss in type 6 crystals (horizontally aligned) is well known for these particles. According to [1] the most probable deposited energy value is 24.513 MeV.

The calibration was done inside the climate chamber at -25°C, with an applied bias voltage of 361.384 V, which corresponds to a DC gain of M= 800, in the high gain branch of the ASIC with a programmable amplification of 32.
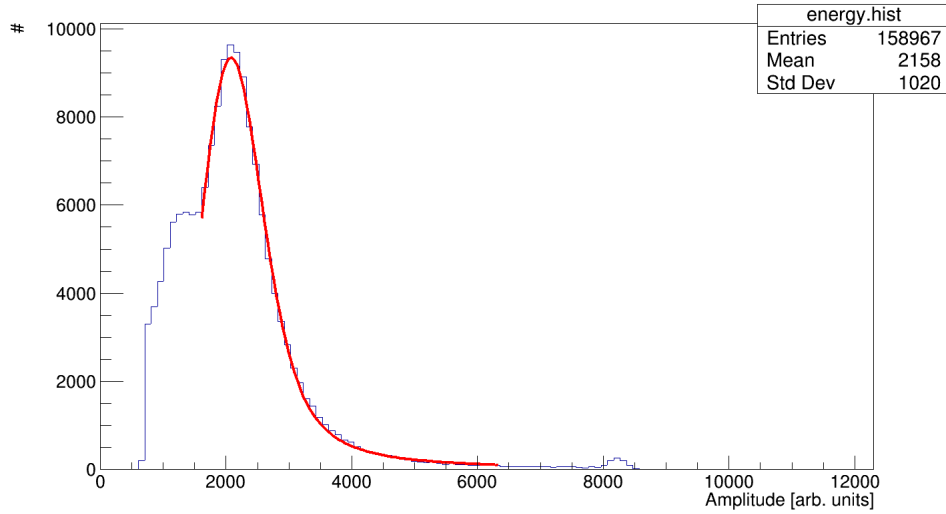
Figure 22: Cosmic muons fitted with a Landau/Gauss convolution.

As seen in fig. 22 the shape of the measured energy spectrum can be described by a convolution of a Landaudistribution and a Gaussiandistribution. The peak of the convolution sits at 2079.526 a.u., with a FWHM of 1182.310 a.u..

These values can be used for a calibration curve, under the assumption that 0 MeV corresponds to an amplitude of 0 and a linear correlation between the pulse height and the deposited energy is given. The smaller peak at around 8230 is due to the limited dynamic range of the readout electronics.

23
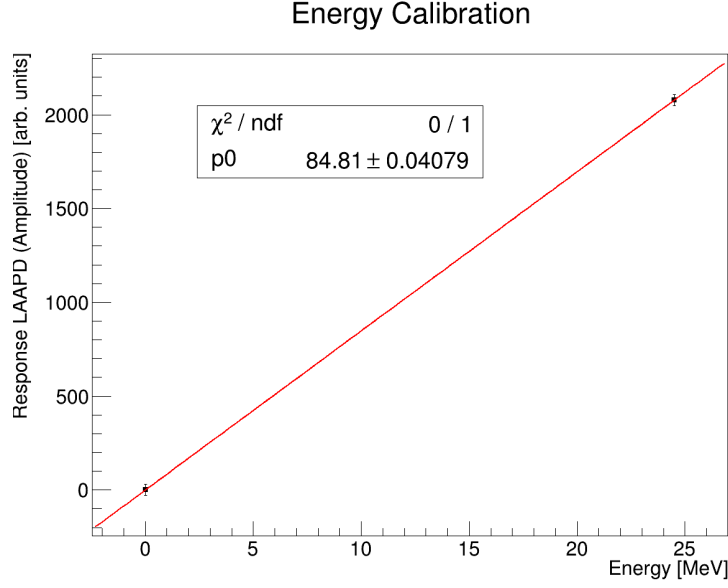
Figure 23: Energy calibration for the setup, with the assumption that 0 MeV corresponds to no signal.

The following equation can be found:

$$A(E) = (84.81 \pm 0.04079) \, \frac{\text{a.u.}}{\text{MeV}} \cdot E \tag{24}$$

Which means

$$E(A) = 0.0118 \, \frac{\text{MeV}}{\text{a.u.}} \cdot A \tag{25}$$

with

$$\Delta E = |\frac{dE}{dA} \cdot \Delta A| = |0.0118 \, \frac{\text{MeV}}{\text{a.u.}} \cdot \Delta A| \approx 0.0005 \, \frac{\text{MeV}}{\text{a.u.}} \tag{26}$$

Therefore, the conversion between pulse height and energy is

$$E(A) = (0.0118 \pm 0.0005) \, \frac{\text{MeV}}{\text{a.u.}} \cdot A \tag{27}$$

3.2 Time Stability of the LED-Pulser

Since the utilized LED-pulser is not intrinsically stabilized, it needs to be warmed up before it can be used with a stable output. For this reason, the time stability of the pulser was tested. As seen in figure 24a, after an initial warm-up phase, the pulser is stable for a period of at least 1.5 h. Figure 24b shows that the pulser needs $\approx 2000 \, \text{s} \approx 33 \, \text{min}$ to reach an appropriate internal temperature stability.

This corresponds to the stability mentioned in [6], which states that it takes about 30 minutes for the pulser to reach an appropriate condition.

(a) Measured stability including the warm-up phase.

(b) Initial warm-up phase.
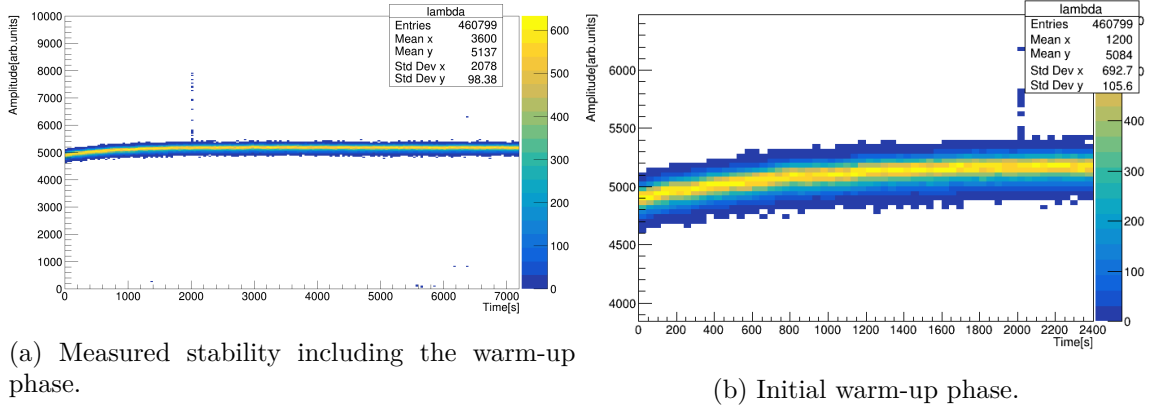
Figure 24: Time stability of the LED-pulser. Measured with the detector inside the climate chamber set to -25 °C.

In order to ensure a stable working condition, the pulser was therefore warmed-up for at least 40 min before each series of measurements.

All measurements that required the same stable amplitude were done without delay.

With a mean pulse heigh of 5163 a.u. and a standard deviation of 75.5 a.u. the deviation of the signal is ≈ 1.46% (see fig. 25a and 25b).

(a) stable area

(b) exemplary Y-Projection
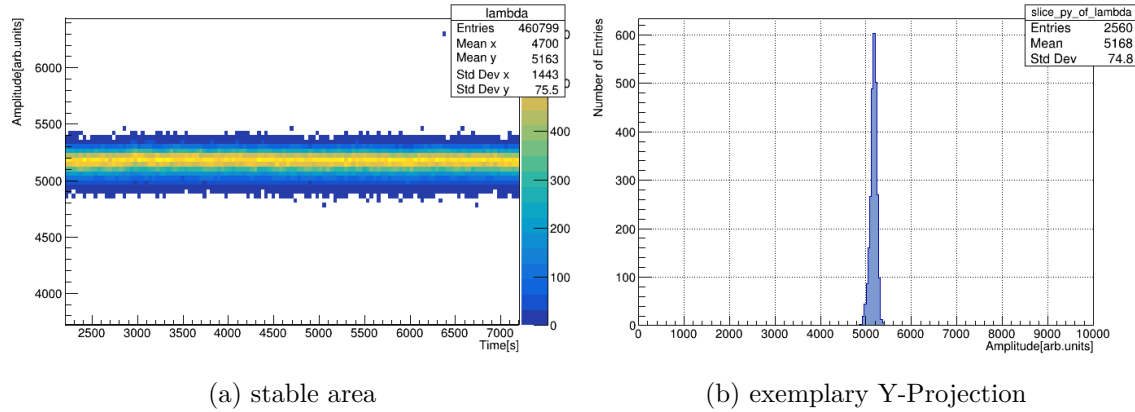
Figure 25: Standard deviation of the pulser signal.

It is noteable that, with an appropriate warm-up time and without an operating climate chamber, the signal has a noticeable drift within the measured two hours (see fig. 26). The deviation here is ≈ 1.15%. This might be due to a thermal drift of the detector. The differences in the deviation might already be effects of the gain used on the resolution.
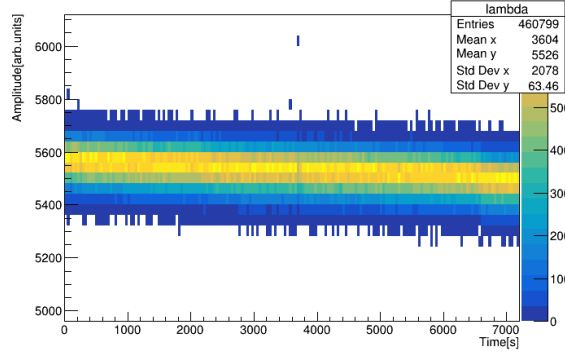
Figure 26: Time stability for a not thermally stabilized detector.
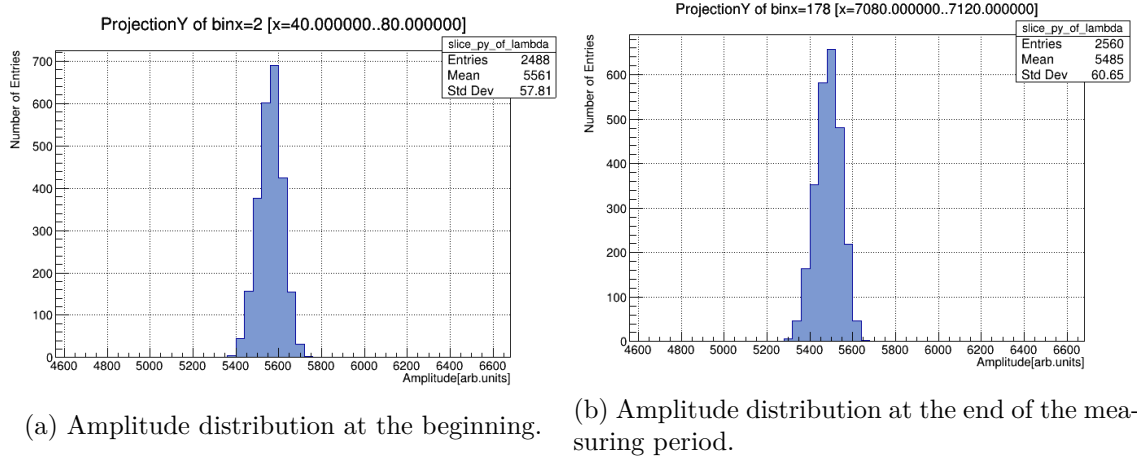
(a) Amplitude distribution at the beginning.

(b) Amplitude distribution at the end of the measuring period.

Figure 27

3.3 Signal Conditioning of the Pulser Signals

For a suitable measurement, the pulser signals should be within the signal range of anticipated energy range of the barrel EMC, with a focus on the low energy side. As a result, the lowest possible intensity should be around 10 MeV and the highest should be close to 1 GeV, at least for the measurements concerning the optimal energy resolution. Above 1 GeV the resolution is not critical due to high photon statistics. Effects like calibration errors or non-uniformities dominate in the higher energy regions. As mentioned before, the plastic fibers have a larger diameter than the optical quartz fibers which are forseen for the P̄ANDA experiment. Since the LED-pulser has been developed for quartz fibers, the light amount transported by the plastic fibers is too high. Even with only one fiber in use and the other nine covered with opaque foil, the signal is even in the low gain branch at the electrical limit of the ASIC, as seen in fig. 28.
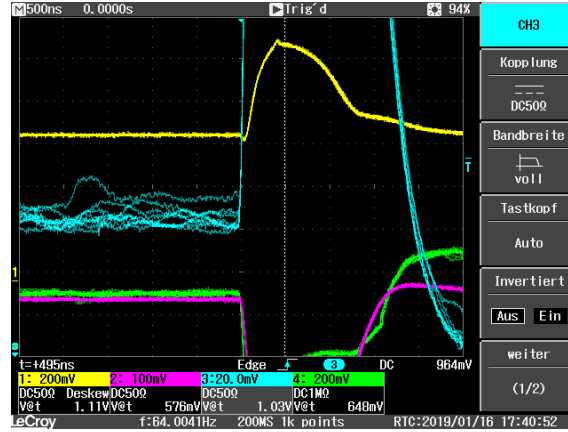
Figure 28: Signal of the LAAPD measured with an oscilloscope, with only one fiber in use. Blue and green show the high gain and yellow and pink the low gain.

In order to decrease the signal, two layers of grey strip foil were put inside the LED-pulser inbetween the optical outlet and the fibers (see fig. 29c).
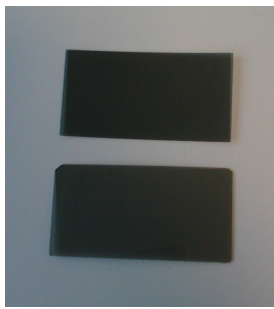
(a) Grey strip foil used as an optical filter.

(b) Attenuation of the foil
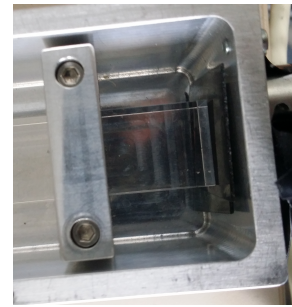
(c) Foil placed inside the pulser.

Figure 29

The attenuation of the foil was not sufficient, since the signal was still at the electrical limit of the readout equipment.
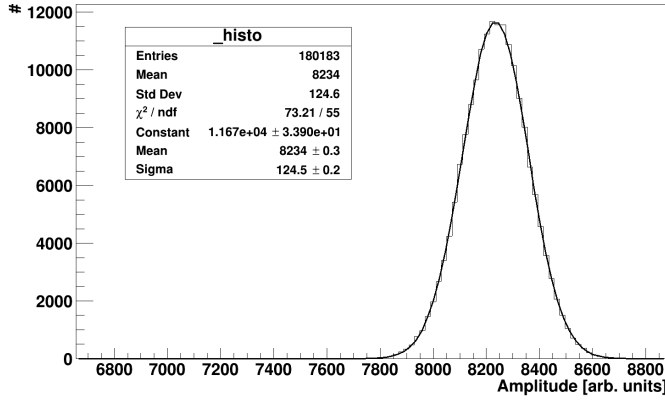
(a) Gaussian fit of the detector signal from the attenuated light pulses. The limit of the SADC is at around a pulse height of 8234 a.u..
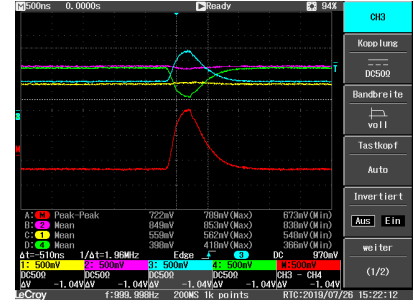
(b) Signal of the detector on the oscilloscope.

Figure 30: Signal of the detector with two layers of foil.

Furthermore, a collimator with a diameter of 0.6 mm was put in front of the fiber.
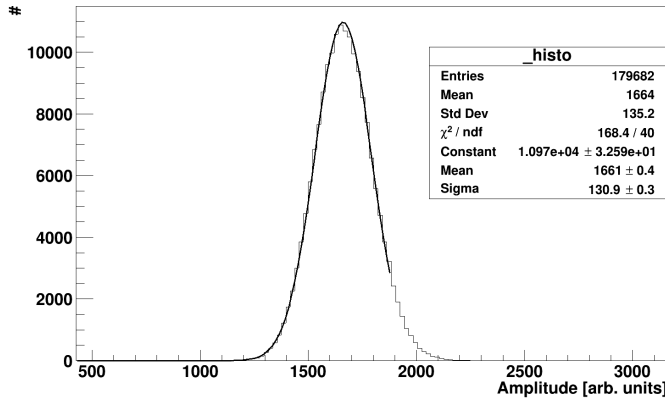
(a) Gaussian fit of the detector signals after applying the collimator.
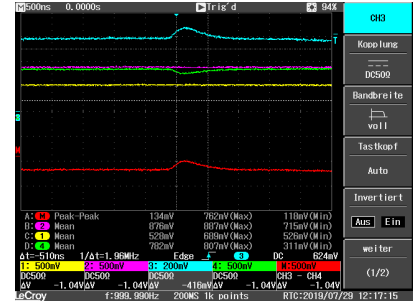
(b) Signal of the detector on the oscilloscope.

Figure 31: Signal of the detector with two layers of foil and an additional collimator.

With the collimator, the amplitude of the smallest signal is equivalent to

$$1661 \, \text{a.u.} \equiv 19.6 \, \text{MeV}. \tag{28}$$

With further attenuation filters inside the LED-pulser, signals lower than

$$1143 \, \text{a.u.} \equiv 13.5 \, \text{MeV} \tag{29}$$

could be reached. The lowest possible energy was $11.3 \, \text{MeV} \pm 1.2 \, \text{MeV}$, which was deemed close enough to the desired 10 MeV:

$$957.9 \, \text{a.u.} \equiv 11.3 \, \text{MeV} \tag{30}$$

This can be seen in fig. 32.

_histo	
Entries	337810
Mean	961.1
Std Dev	123.3
χ^2 / ndf	243.4 / 18
Constant	$1.279e+04 \pm 4.195e+01$
Mean	957.9 ± 0.3
Sigma	115.1 ± 0.3
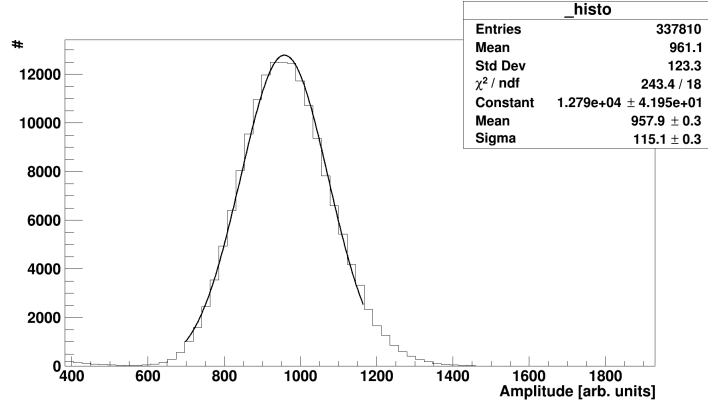
Figure 32: Lowest possbile signal of the setup.

3.4   Linearity between High Gain and Low Gain

Due to the limited dynamic range of the readout equipment, both high gain branches and the low gain branch have to be used. The difference of the selectable high gain amplification is a factor of two. While they are supposed to be amplified relatviely to the low gain branch (with no further amplification) by a factor of 16 and 32 respectively, the true values are lower.

In order to retain a way of converting pulse height to energy equivalent, the real amplification values have been determined. For these measurements, two layers of foil as well as a collimator were used to decrease the pulser signal. The transmittance was set to a value of 900 DAC a.u. and decreased in steps of 50 a.u. for each step, with a pulse frequency of 2 kHz.

Each setting was measureed with the SADC for 90 s.

The LAAPD was operated at 361.384 V. In order to be able to measure low gain signals and high gain signals simultaneously, the high gain branch amplification was set to 16.
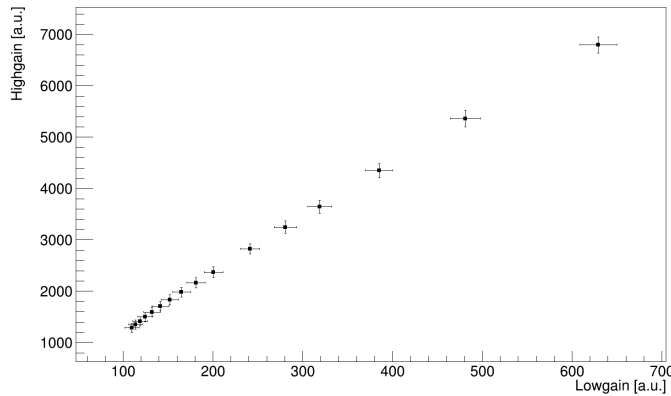
Figure 33: High gain signal with an amplification of 16 plotted against the low gain signals for the same pulser intensities.

As it can be seen from fig. 34 the high gain branch and the low gain branch show a

non-linear behavior for higher energies.

(a) Linear fit of high gain against low gain.

(b) Residual between the measured high gain and the linear fit in MeV.
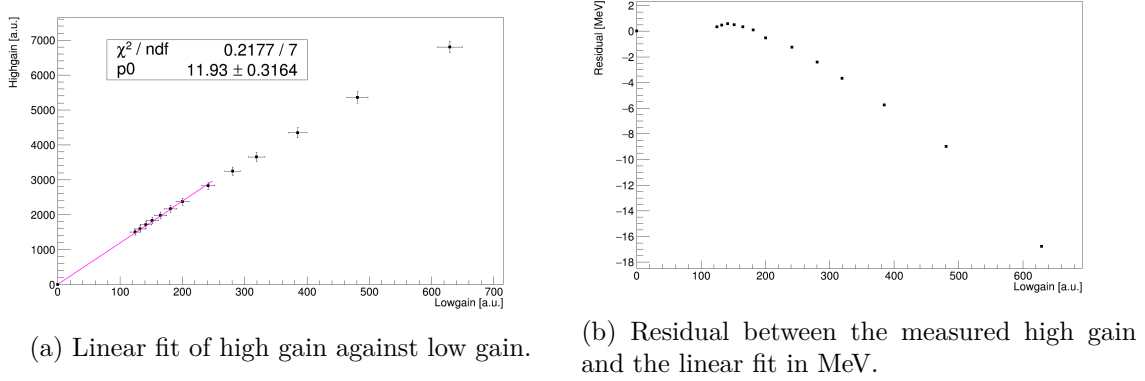
Figure 34

If the non-linear behaviour is considered, the residual in MeV is significantly lower. The non-linear behaviour can be described by the following equation

$$f(x) = P_0 \cdot (1 - e^{-\frac{x}{P_0}}) \cdot P_1 \tag{31}$$

where f describes the high gain at a set amplification of 16 and x the low gain.

(a) Non-linear fit of high gain against low gain.

(b) Residual between the measured high gain and the non-linear fit in MeV.
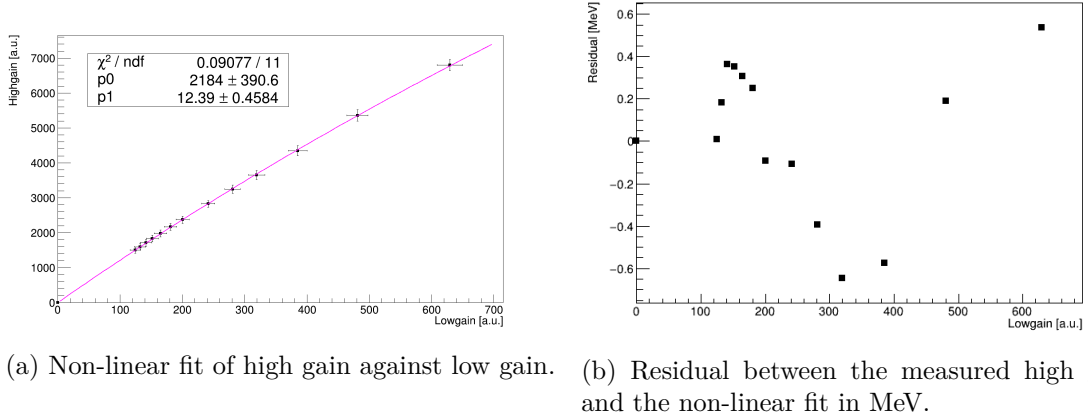
Figure 35

The linear contribution to the function is described by P_1. As can bee seen in fig. 35a the linear contribution is approximately 12 and not the expected 16.

Since the residuals are significantly lower for the non-linear fit, it was used to extrapolate between high gain and low gain. Especially since the highest signal for this measurement corresponds to roughly 160 MeV and the optimization measurements are supposed to be in a range of up to 1 GeV, where the non-linear contribution becomes more significant.

3.5   In-Situ Characterization of the LAAPD

In order to convert between the units energy calibration at an assumed gain of M = 800 and every other gain, one should be able to assume a linear correlation between the signal

for a set light intensity of the LED-pulser and the gain. In order to verify this connection, the pulse height for a set light intensity (731 DAC a.u) was measured for different gains with the characterization supplied by the PSL, seen in fig.15.
The following behavior was observed:
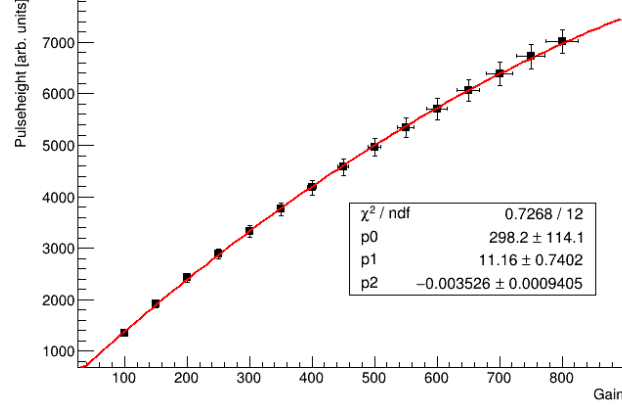
Figure 36: Pulse height of the LED-pulser vs. the LAAPD gain. A second degree polynomial trend was observed.

(a) Measurement up to M=400 with a linear fit.

(b) Measurement up to M=400 with a second degree polynomial fit.
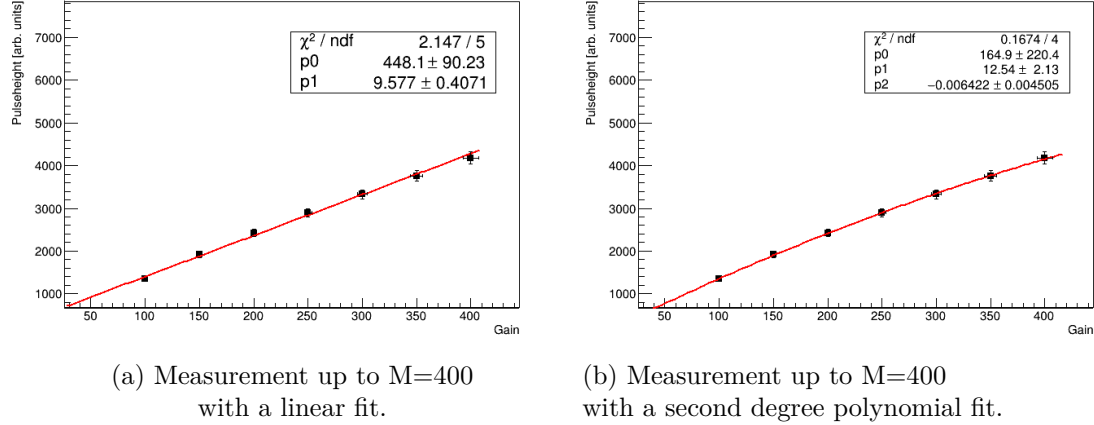
Figure 37

As seen in fig. 36 and especially in fig. 37 the pulse height does not decrease in a linear fashion but seems to have a second degree polynomial connection to the gain. The utilized LAAPD was characterized by the PSL in Darmstand during the end of a long research and development phase. The same measurement was conducted with a new $\bar{\mathrm{P}}$ANDA detector matrix, using LAAPDs characterized by the university of Bochum. The same readout was used.
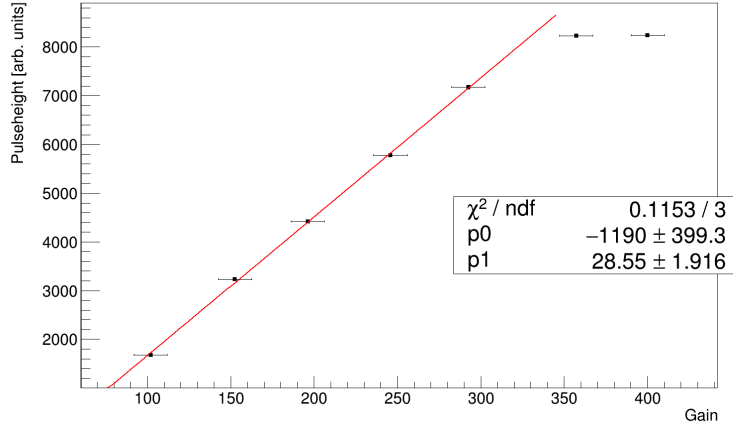
Figure 38: Pulse height of the LED-Pulser against the set gain, measured with an APD characterized in Bochum.

Both APDs show a non-linear trend when operated with the given characteristics. This means that the actual gain-voltage-curve and the assumed gain-voltage-curve do not match.

This effect has already been described by Oliver Noll as reported to the $\bar{\text{P}}$ANDA-Collaboration[8]. The input capacitance of the APFEL-ASIC acts as a charge divider. This effect does not change the behavior of the LAAPD significantly under continuous illumintaion (DC). However, if a pulsed signal is used (AC), the capacitance of the LAAPD is dependent on the voltage, which in turn has an effect on the gain-to-voltage relation.
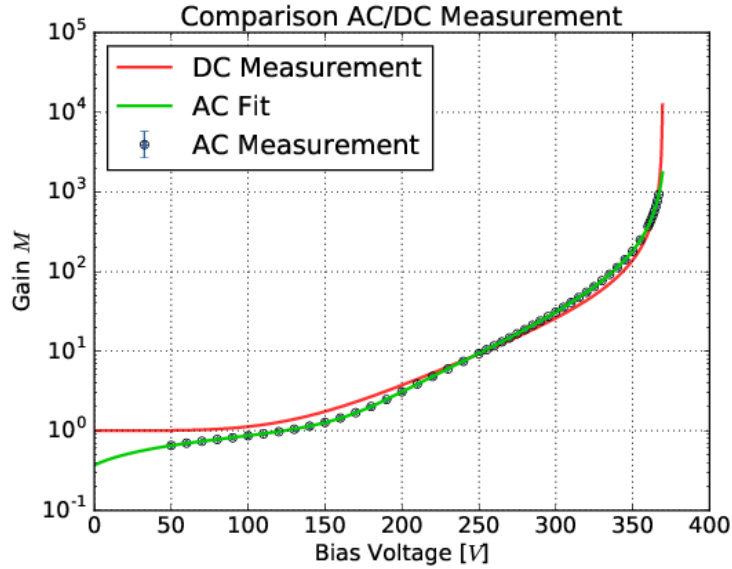
Figure 39: Difference in AC-characterization and DC-characterization of an LAAPD[8].

As seen in fig. 39, the gain curve does not form a plateau for lower voltages and the shape differs from the Miller function (eq. 23).

In principle, it is possible to do an in-situ characterization of the LAAPD with the given

setup. Due to the limited range, it is not possible to measure the complete curve for a single intensity. If done correctly, parts of the curve can be measured for different intensities. If the overlap between these areas is sufficient, the curves can be merged and a complete curve is created.
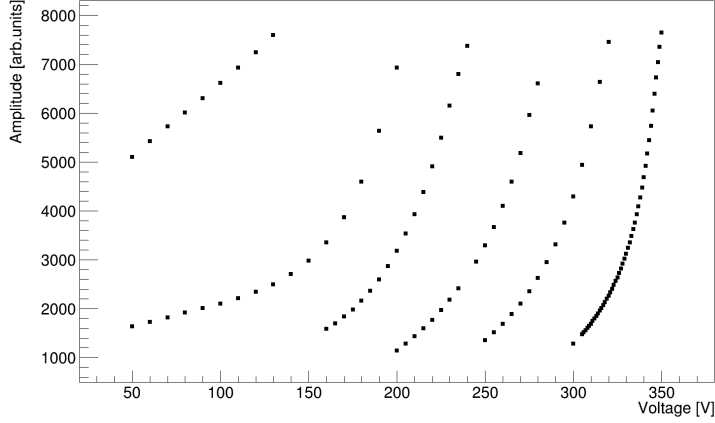
Figure 40: Measured curves for different light pulser intensities.
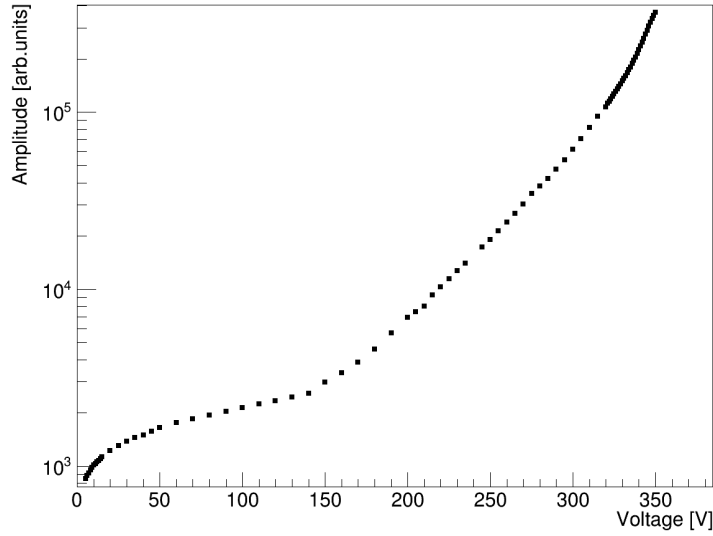
Figure 41: Merged measurements. There is no plateau which indicates $M = 1$.

It is possible to measure the AC characteristics of the LAAPD with a running setup, however, it is important to measure the overlap in certain areas carefully in order to ensure a smooth transition between measurements.
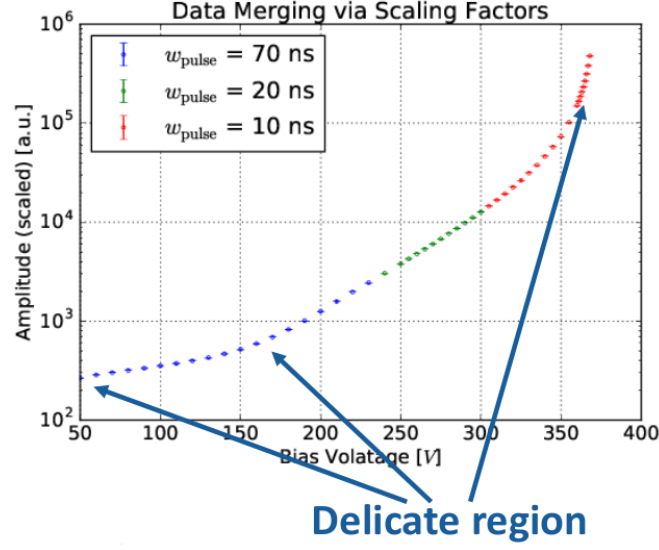
Figure 42: Merged traces with an indication of delicate areas where the overlap bewteen measurements should be as large as possible and where the voltage has to be measured carefully[8].

$M = 1$ cannot be defined like for the DC characterization. It is therefore necessary to extrapolate the DC characteristics from the measured AC ones in order to attribute an amplitude to $M = 1$.

This is done with the following equation[8]

$$F_{fit}(U, A, U_b, \alpha, a, b, c, d, e, R) = \frac{R \cdot f_{DC}(U, A, U_b, \alpha)}{1 + C_d(U, a, b, c, d, e)}. \tag{32}$$

Where F_{fit} is the curve fitted to the AC characterization and f_{DC} is the known Miller function for continuous illumination. C_d describes the relation between capacitance of the detector and the LAAPD bias voltage. These characteristics have already been measured for a few selected LAAPDs, but since the behaviour for individual LAAPDs does not deviate significantly, it is sufficient to find a suitable function for a selected one.

The relation between the capacitance and the bias voltage can be described by[8]

$$C_d(U, a, b, c, d, e) = C_1(U, a, b) + C_2(U, c, d, e) \tag{33}$$

with C_1 describing the general behaviour and C_2 describing the kink at a certain voltage.

$$C_1(U, a, b) = \frac{a}{\sqrt{1 + b \cdot U}} \qquad C_2(U, c, d, f) = \frac{f}{1 + e^{-c \cdot (U - d)}} \tag{34}$$

In principle, C_d can be found, by first fitting the data points with C_1, then plotting the residual of the measured data and the found function and fit the residual with C_2.

When the found parameters are used as fitparameters for C_d, a curve that describes the data well is found.
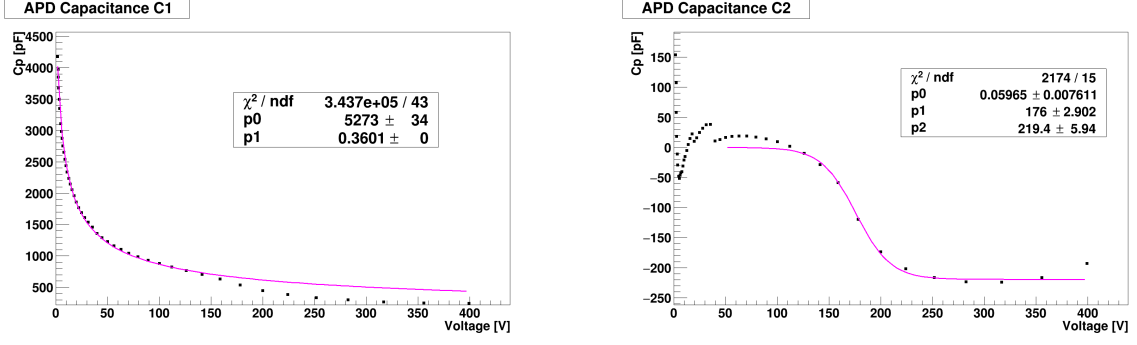
(a) Measurement for an LAAPD that has been through the irradiation process with C_1.

(b) Residual of the measured data and C_1 fitted with C_2.

Figure 43
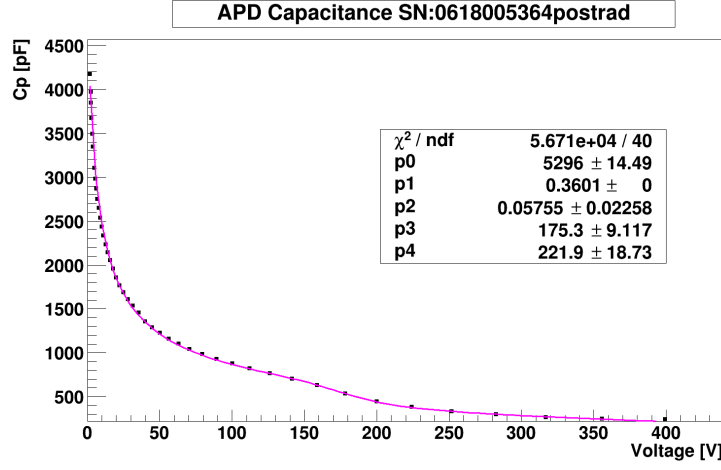
Figure 44: Detector capacitance as a function of the bias voltage of the LAAPD, fitted with C_d.

Even though the characteristics were measured, it was not possible to find a suifficient fit for the data.
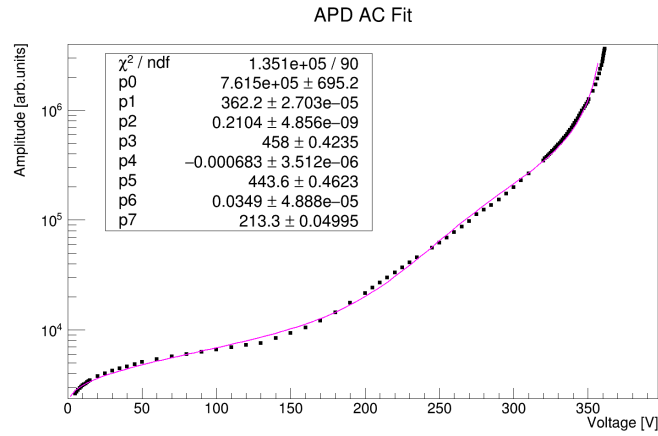
Figure 45: Measured data points where every parameter is taken into consideration.

The "best" fit that could be found is shown in fig. 45. This fit does not give an accurate enough DC characterization. Due to time constraints an alternative approach was used. Instead of measuring the optimum gain, the optimum voltage applied to the LAAPD was determined, since the gain-to-voltage correlation is fixed and the energy calibration is known for U = 361.384 V.

3.6 Gain Measurements

The optimal energy resolution was determined at seven different energies.
For most intensities the energy was determined at a bias voltage of 361.384 V, since the energy calibration was done at the same voltage.
Because the amplification factors between the two high gain amplifications and the low and high gain branches is known, the calculated energy calibration could be used up to an energy equivalent of 558.7 MeV, since for higher energies even the low gain branch is at the electrical limit of the readout electronics.
For the energies that were measured at a high gain amplification of 32, the pulse height can be simply converted into an energy equivalent by using the factor that has been found in ch. 3.1. The measurements can be seen in fig. 46a, 46b and 46c.

$$957.9\,\text{a.u.} \cdot 0.0118\,\frac{\text{MeV}}{\text{a.u.}} = 11.30\,\text{MeV} \tag{35}$$

$$3096\,\text{a.u.} \cdot 0.0118\,\frac{\text{MeV}}{\text{a.u.}} = 36.53\,\text{MeV} \tag{36}$$

$$4986\,\text{a.u.} \cdot 0.0118\,\frac{\text{MeV}}{\text{a.u.}} = 58.83\,\text{MeV} \tag{37}$$

(a) 11.3 MeV

(b) 36.5 MeV

(c) 58.8 MeV
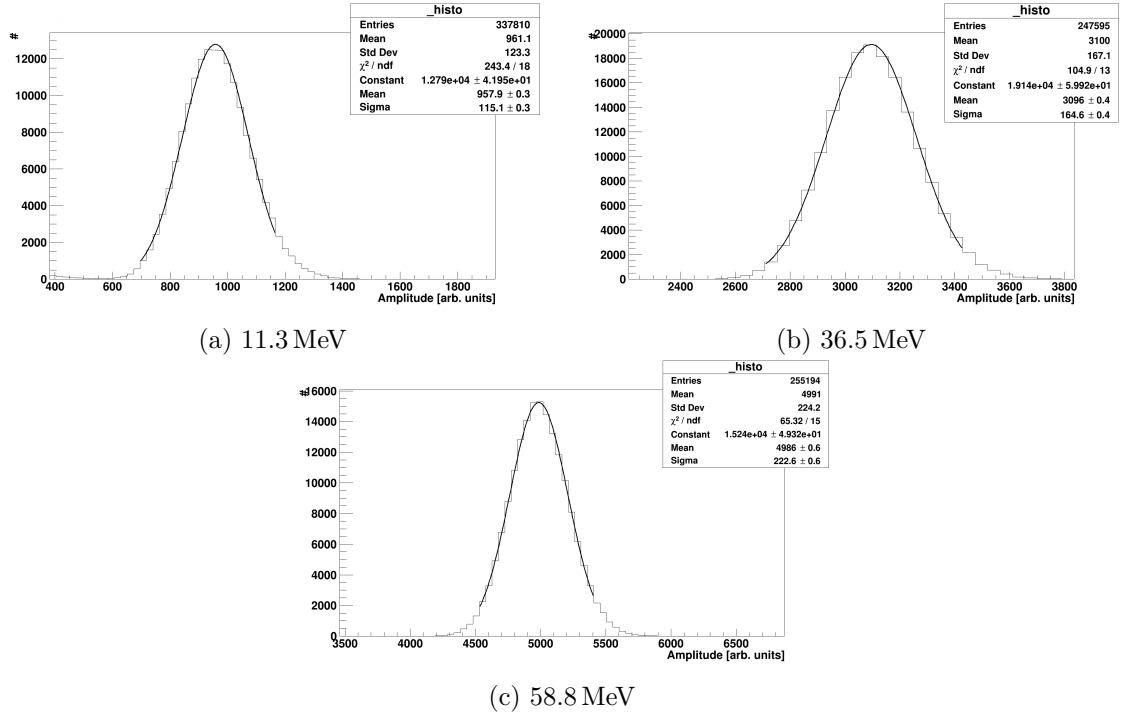
Figure 46: Energies measured with a high gain amplification of 32 at a bias voltage of 361.384 V. The number of counts is plotted against the pulse height.

Even though the amplifications for the high gain branches are not 16 and 32, the factor between the two settings is 2. This means that for the ch.amp x16 setting every amplitude is only half as high as for the x32 setting. This means the conversion factor into an energy is simply the already calculated factor multipliedby a factor of two.

$$4539 \, \text{a.u.} \cdot 2 \cdot 0.0118 \, \frac{\text{MeV}}{\text{a.u.}} = 107.12 \, \text{MeV} \tag{38}$$

The measured amplitude can be seen in fig. 47.
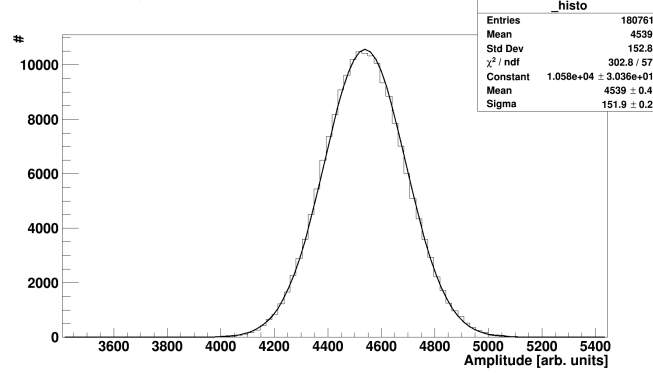
Figure 47: Energy measured with a high gain amplification of 16 at a bias voltage of 361.384 V. The number of counts is plotted against the pulse height.

For the energies measured in the low gain branch, the non-linearity between high and low gain has to be taken into consideration. Instead of multipliying a constant factor, the multplication has to be done with:

$$A_{16} = 2184 \cdot (1 - e^{-\frac{A_{lg}}{2184}}) \cdot 12.39 \tag{39}$$

The calculated amplitude can then be converted into an energy equivalent by using the factor for the x16 high gain branch:

$$2184 \cdot (1 - e^{-\frac{1215}{2184}}) \cdot 12.39 \cdot 2 \cdot 0.0118 \, \frac{\text{MeV}}{\text{a.u.}} = 272.48 \, \text{MeV} \tag{40}$$

See also fig. 48a.

$$2184 \cdot (1 - e^{-\frac{4539}{2184}}) \cdot 12.39 \cdot 2 \cdot 0.0118 \, \frac{\text{MeV}}{\text{a.u.}} = 558.69 \, \text{MeV} \tag{41}$$

See also fig. 48b.

(a)

(b)
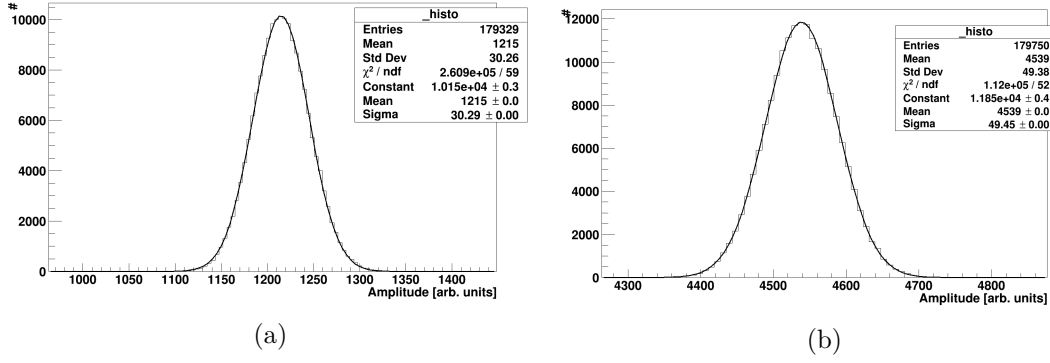
Figure 48: Measured energies in the low gain branch at a bias voltage of 361.384 V. The number of counts is plotted against the pulse height.

For higher intensities, the energy can no longer be determined at a bias voltage of 361.384 V, since the signal will be in saturation even in the low gain branch. In order to still be able to get data for energies > 1 GeV, an intensity was chosen, where the low gain signal was still visible for the energy calibrated bias voltage and a voltage at a much lower amplification. The intensity of the pulser was set to an equivalent of ≈ 560 MeV and a bias voltage was selected so that the pulse height would be around $\frac{1}{4}$ of the signal at 361.384 V.
The selected voltage was 349.194 V which corresponds to a gain of 180 in the DC characterization.

(a) Measured intensity at 361.384 V.

(b) Intensity from (a), measured at 349.194 V.
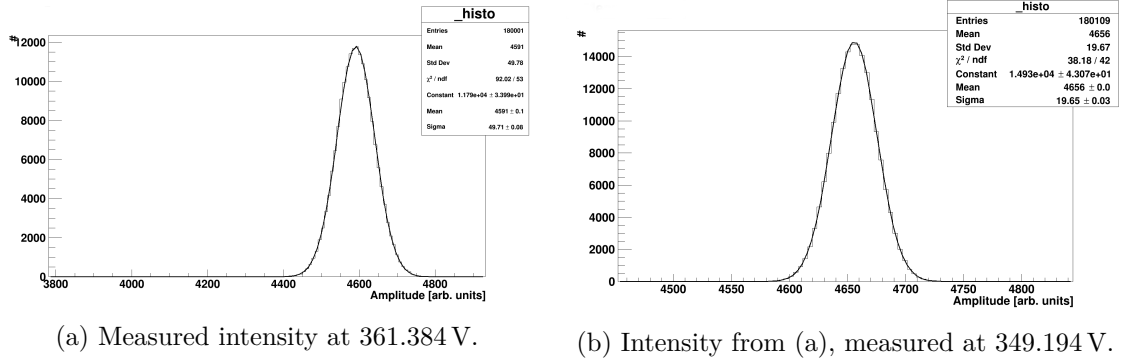
Figure 49

The ratio between the two selected bias voltages is calculated by dividing the two measured amplitudes, as seen in fig. 49:

$$\frac{4591 \, \text{a.u.}}{1383 \, \text{a.u.}} = 3.32 \tag{42}$$

The intensity was then set to an intensity where the pulse height at a bias voltage of 349.194 V was around the same value as for 361.384 V, which can be seen in fig. 50. The corresponding energy can be calculated by:

$$2184 \cdot \left(1 - e^{-\frac{4656}{2184}}\right) \cdot 12.39 \cdot 3.32 \cdot 2 \cdot 0.0118 \, \frac{\text{MeV}}{\text{a.u.}} = 1869.47 \, \text{MeV}. \tag{43}$$

_histo	
Entries	180109
Mean	4656
Std Dev	19.67
χ^2 / ndf	38.18 / 42
Constant	1.493e+04 ± 4.307e+01
Mean	4656 ± 0.0
Sigma	19.65 ± 0.03
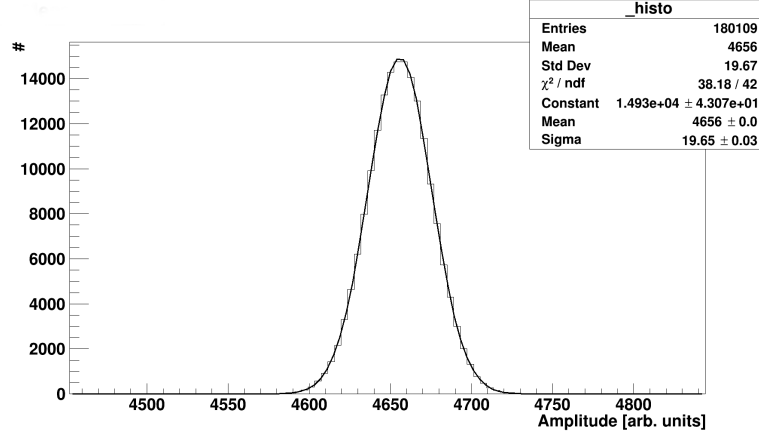
Figure 50: Highest intensity measured at 349.194 V, with a mean amplitude of 4656 a.u.

For 11.3 MeV the voltages were chosen in what would have been 20 steps in gain for the DC characterization. For 36.52 MeV up to 558.69 MeV, voltages were chosen which would have corresponded to 50 steps in gain, with additional measurements around the minimum resolution. For 1.8 GeV a step width of 10 was chosen, starting at what would be $M = 180$.

The measured data can be seen in fig. 51 and an overview over the configurations used as well as the minimal measured energy resolution can be found in table 3.

(a)

(b)

(c)

(d)

(e)

(f)

(g)
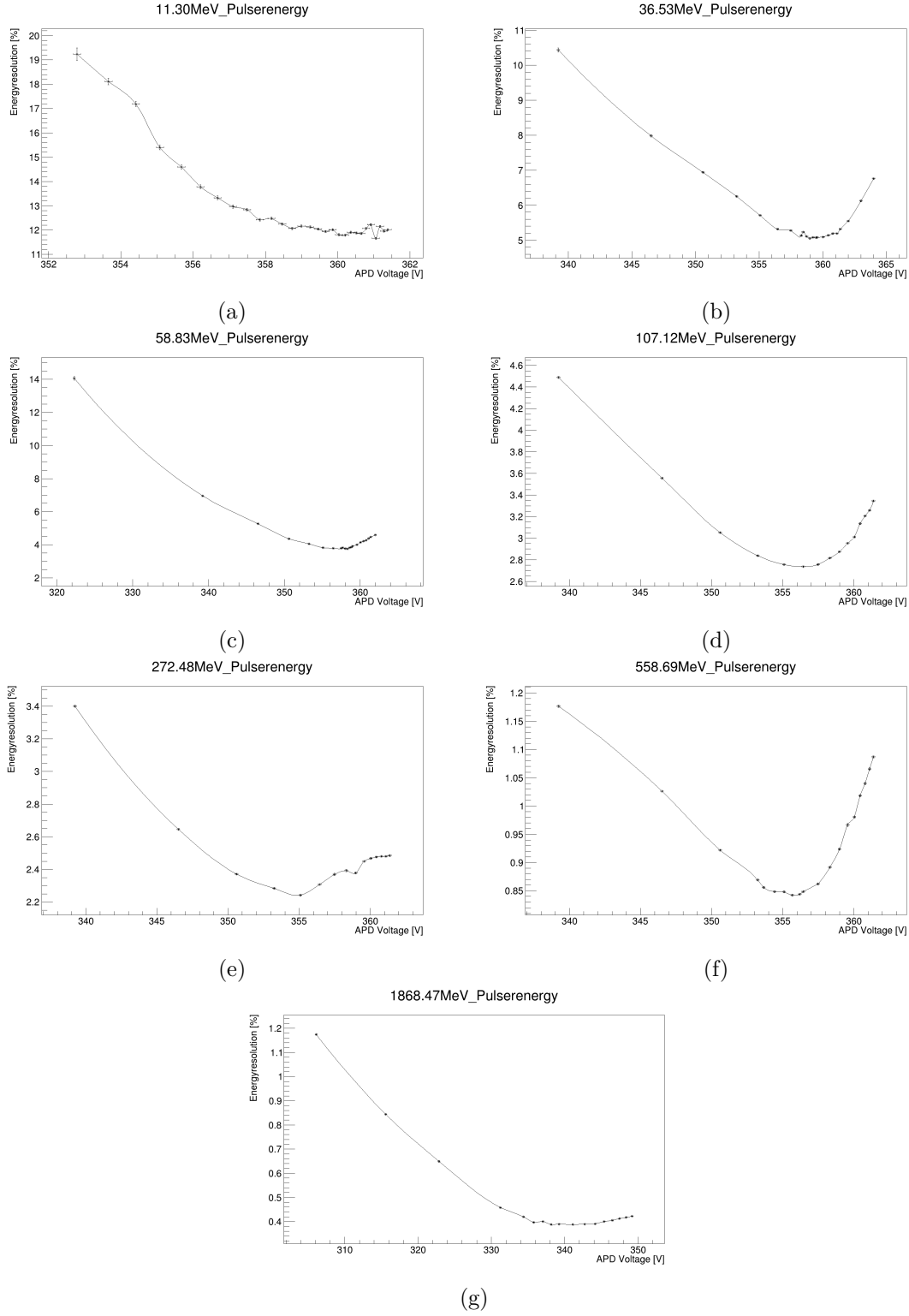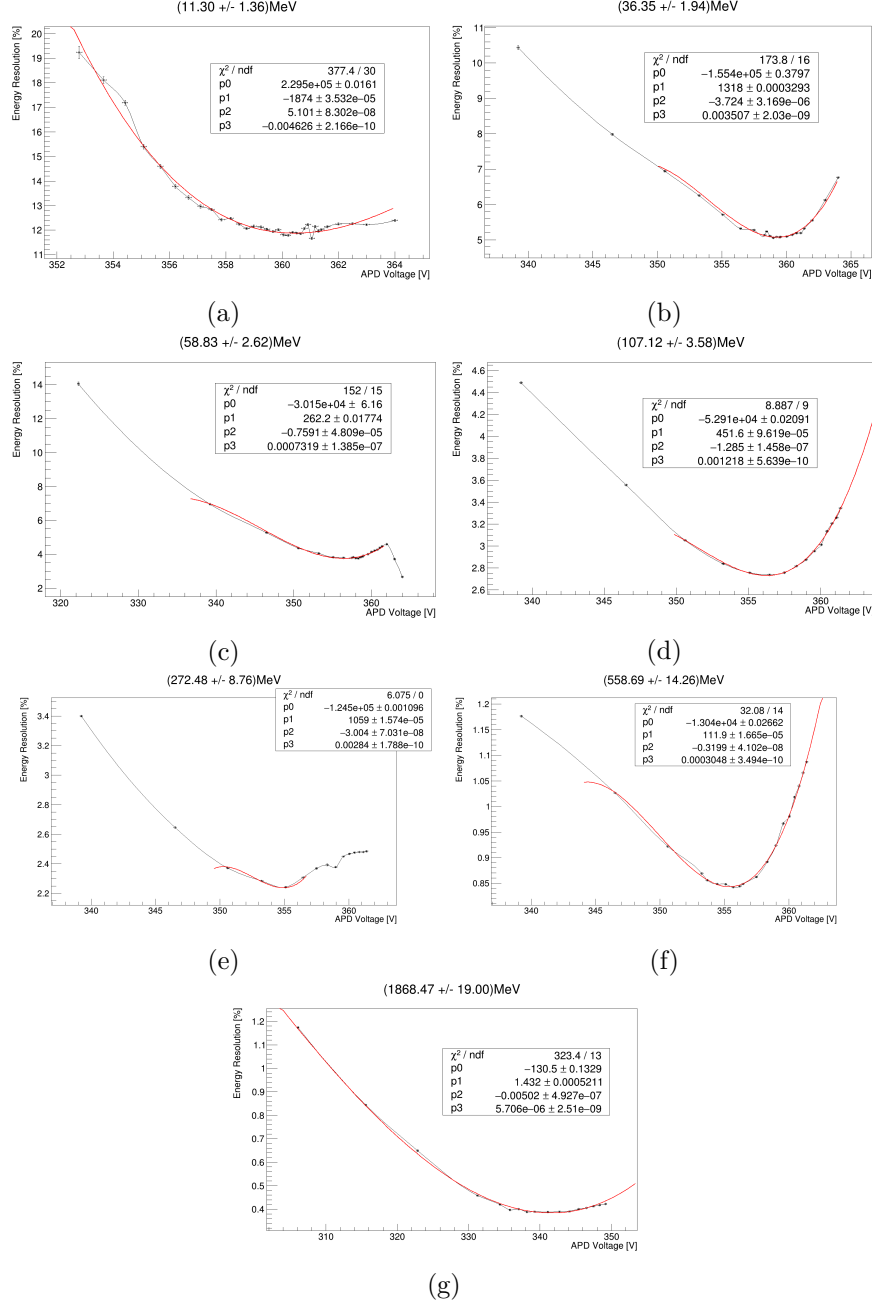
Figure 51: Measurements for the optimal gain resolution. Plotted is the energy resolution in % as a function of the applied bias voltage, including an interpolation of the data points.

Energy equiv.[MeV]	Attenuation	Ch. Amp.	$(\sigma/E)_{min}[\%]$	$U_b[V]$
11.30 MeV	2 foils, attenuator, 0.6 mm collimator	high gain x32	11.66	361.06
36.53 MeV	2 foils, attenuator, 0.6 mm collimator	high gain x32	5.05	358.99
58.83 MeV	2 foils, attenuator, 0.6 mm collimator	high gain x32	3.76	358.32
107.12 MeV	2 foils, attenuator, 0.6 mm collimator	high gain x16	2.74	356.44
272.48 MeV	2 foils, 0.6 mm collimator	low gain	2.24	355.08
558.69 MeV	2 foils, 0.6 mm collimator	low gain	0.84	355.67
1869.47 MeV	0.6 mm collimator	low gain	0.39	341.10

Table 3: Overview over the measured energies and utilized configurations, as well as the minimal measured energy resolution and the corresponding bias voltage.

3.7 Noise

As can be seen for the 11.3 MeV measurement, at some bias voltages in the lower region no measurements were made. This is because lower signals could not be distinguished from random peaks of the noise spectra.
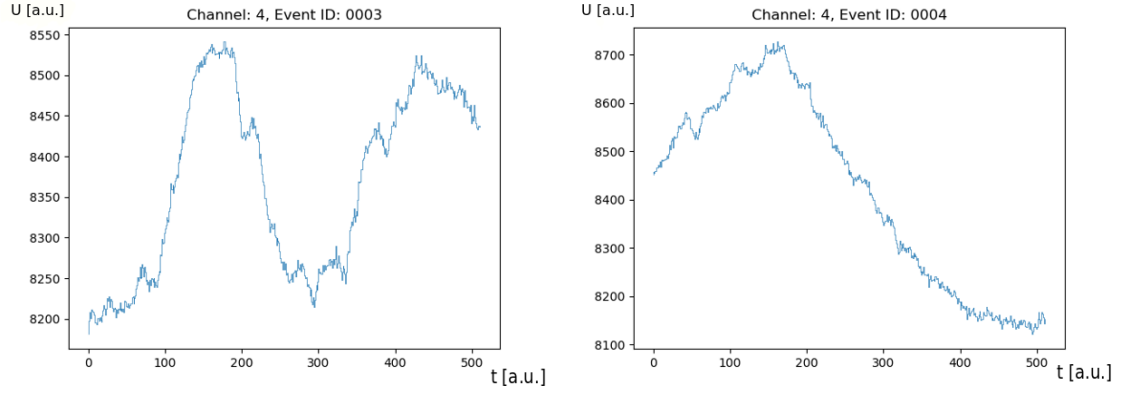
(a) Fluctuations of the baseline for trace 3.

(b) Fluctuations of the baseline for trace 4.
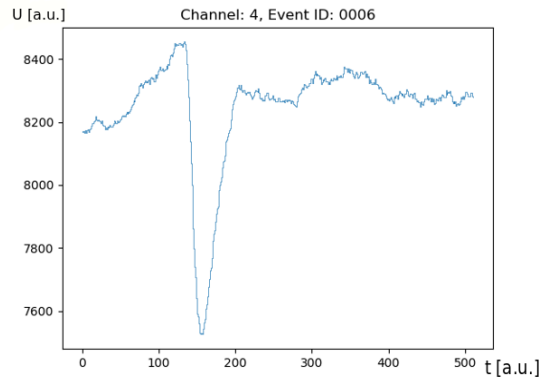
(c) A signal of the LED-pulser.

Figure 52: Raw traces of the measurement at 58.8 MeV with a bias voltage of 339.222 V. Plotted is the voltage signal in arbitrary units against the bin, which corresponds to time.

The self-triggering SADC calculates a floating baseline. The trigger threshold was set set

400 a.u. away from the baseline. This corresponds to a value of roughly 4.72 MeV. This noise level stayed constant at different gain and energy settings.

In case of a clear signal from the LED-pulser, via using a sufficient APD gain, the floating noise level was observed:
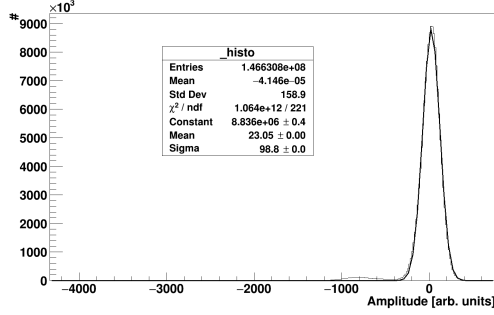
(a) Noise for 11.3 MeV pulses with a bias voltage of 361.348 V.
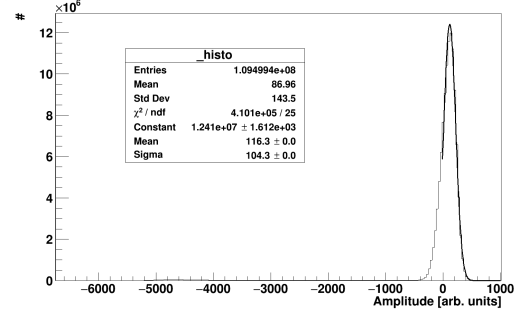
(b) Noise for 58.8 MeV pulses with a bias voltage of 361.348 V.
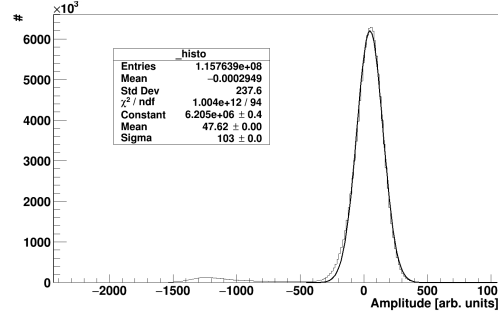
(c) Noise for 58.8 MeV pulses with a bias voltage of 346.507 V.

Figure 53: Selected noise measurements for different energies and bias voltages. A higher energy was selected as well, because $M_{DC}=150$ (346.507 V) could not be measured at 11.3 MeV

The noise was calculated by subtracting the measured trace from the calculated baseline, while the traces of the signal were omitted from the calculation.

At an energy of 11.3 MeV for a bias voltage of 361.348 V the noise corresponds to an energy of:

$$23.05 \,\text{a.u.} \cdot 0.0118 \,\frac{\text{MeV}}{\text{a.u.}} = 0.27 \,\text{MeV}, \tag{44}$$

while the noise for the same bias voltage at 58.8 MeV corresponds to

$$116.3 \,\text{a.u.} \cdot 0.0118 \,\frac{\text{MeV}}{\text{a.u.}} = 1.37 \,\text{MeV} \tag{45}$$

As can be seen, the noise level increases between the two measurements. However, there was a day of delay between the two measurements, so it might be possible that the LAAPD picked up some noise from the lab.
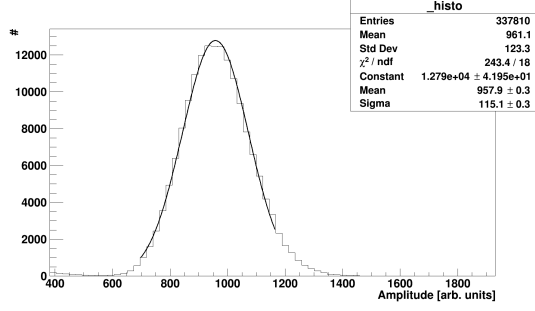
(a) Signal for 11.3 MeV pulses with a bias voltage of 361.348 V.
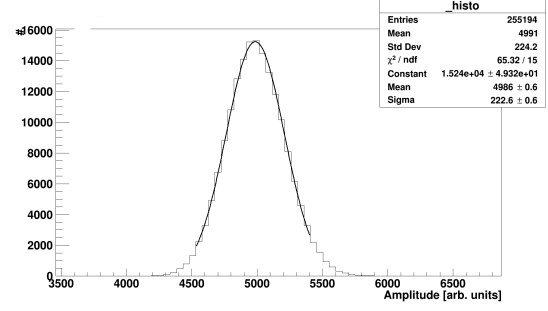
(b) Signal for 58.8 MeV pulses with a bias voltage of 361.348 V.
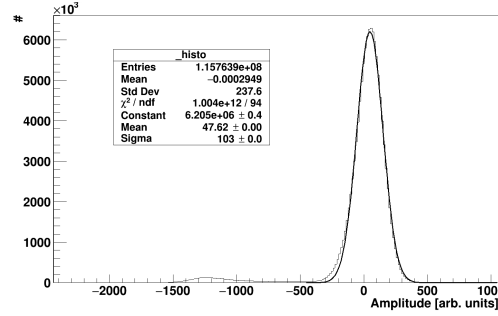
(c) Signal for 58.8 MeV pulses with a bias voltage of 346.507 V.

Figure 54: Signals for the selected measurements

The signal to noise ratio for the two selected bias voltages and enegry settings is as follows:

$$\frac{S}{N}(361.384\,\text{V})@11.3\,\text{MeV} = \frac{957.9\,\text{a.u.}}{23.05\,\text{a.u}-} = 41.6 \tag{46}$$

$$\frac{S}{N}(361.384\,\text{V})@58.8\,\text{MeV} = \frac{4986\,\text{a.u.}}{116.3\,\text{a.u}-} = 42.9 \tag{47}$$

$$\frac{S}{N}(346.507\,\text{V})@58.8\,\text{MeV} = \frac{1362\,\text{a.u.}}{47.62\,\text{a.u}-} = 32.7 \tag{48}$$

While the signal to noise ratio bewteen the two bias voltages changes significantly, which is expected, as the ratio significantly depends on the gain, the difference in signal to noise ratio between the two energies for the same bias voltage is negligible.

4 Data Analysis

In order to find the optimum energy resolution for each chosen energy, the measured resolution is plotted against the LAAPD voltage.

Figure 55: Measurements for the optimal gain resolution. Plotted is the energy resolution in % as a function of the applied bias voltage.

The data was fitted with a third degree polynomial, see fig. 55. Since the minimal energy resolution is of interest, the fit range was restricted around the lowest measured resolution. From these fits the minimum was calculated. As expected, the energy resolution improves with higher energies.

Energy equiv.[MeV]	$(\sigma/E)_{min}[\%]$	$U_b[\text{V}]$
11.30 MeV	11.9	360.29
36.53 MeV	5.07	356.42
58.83 MeV	3.76	358.32
107.12 MeV	2.73	356.24
272.48 MeV	2.24	354.9
558.69 MeV	0.85	355.4
1869.47 MeV	0.38	341.52

Table 4: Overview over the selected energies and the minimum energy resolution as well as the corresponding bias voltage calculated from the fit.
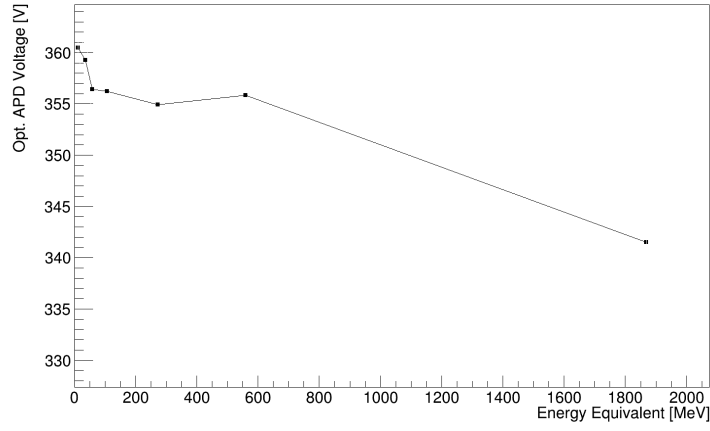
Figure 56: Optimum bias voltage in terms of energy resolution.

5 Discussion and Outlook

Because the in-situ (AC) characteristics of the LAAPD could not be converted from amplitude to gain, as no plateau indicating gain 1 was found, all statements about the gain can only be taken from the characteristics measured under continuous illumination (DC). One has to keep in mind, that the DC characterization shows a deviation from the actual gain and can only be considered as an approximation. For correct statements the AC characterization needs to be done.

Nevertheless, the settled screening process for the $\bar{\text{P}}$ANDA experiment uses a DC characterization. Therefore, the gain statements in this chapter could be taken as guidelines for the operation of the $\bar{\text{P}}$ANDA barrel calorimeter.

5.1 Optimum Gain for the Full Energy Range
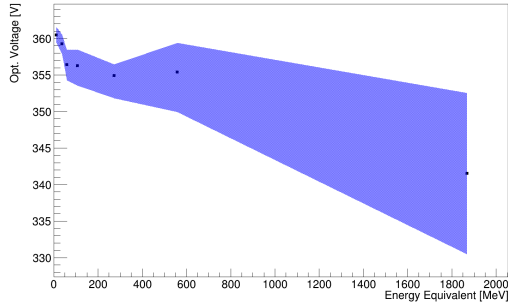
(a) Evaluation with a 0.1% resolution loss tolerance band.
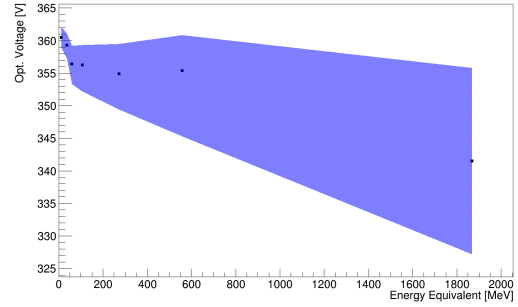
(b) Evaluation with a 0.2% resolution loss tolerance band.

Figure 57: Optimmum bias voltage in terms of energy resolution of the LAAPD plotted against the energy equivalent. The shaded areas indicate the resolution loss tolerance bands. Due to missing data at 1.89 GeV, the upper limit of the resolution loss tolerance band was deduced from symmetry considerations.
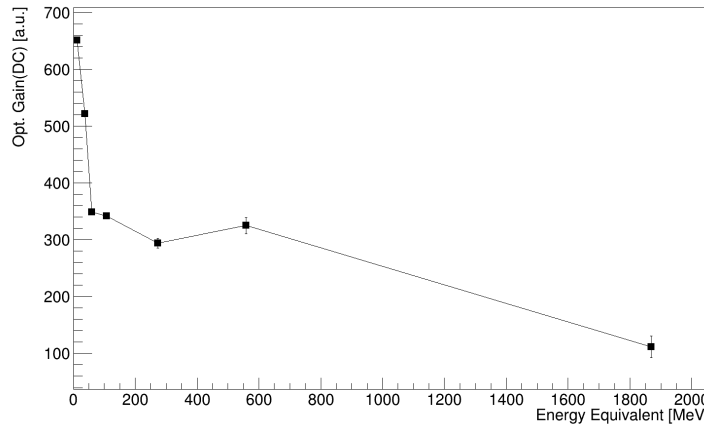
Figure 58: Optimum DC gain in terms of energy resolution.

46

As can be seen, the optimum voltage, as well as the optimum gain, decrease with higher energies.

In order to find an optimum setting which is sufficient over a wide range, one has to set some priorities first. On the one hand, the energy resolution above 1 GeV is not dominated by the LAAPD gain. For high energies, the response parametrization found in ch. 1.2.3 is dominated by the constant term[3], this means for higher energies inhomogeneities and inaccuracies will mostly be of importance for the energy resolution and not the factors effected by the photon statistics and the excess noise factor, which play a role for the gain used.

On the other hand, below 1 GeV the energy resolution has to be sufficient over a wide range of energies.

Because the gain changes more significantly with small changes of the bias voltage for higher voltages, one should also consider how much resolution one loses if a lower voltage is chosen. A small change at a higher voltage has a higher impact on the energy resolution than a small change for a lower voltage. Therefore lower energies carry a greater weight for the energy resolution.

In order to define an optimum resolution voltage a tolerance band of 0.2% resolution loss was chosen. As a optimum energy resolution voltage 359 V was chosen.
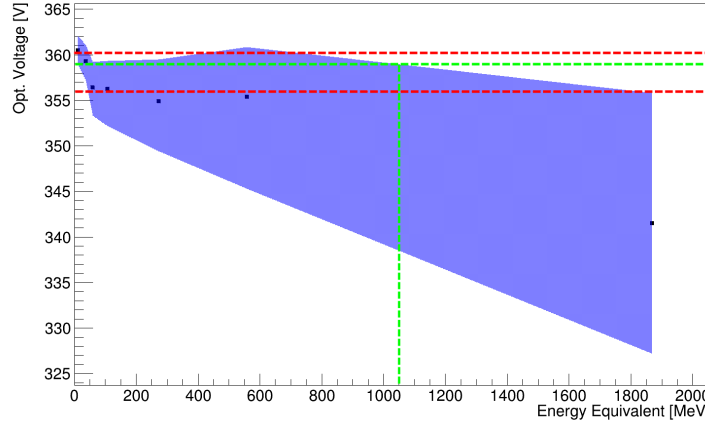
Figure 59: Optimum energy resolution. The shaded area represents a 0.2% resolution loss tolerance. The red lines show the chosen limits for the optimal voltage and the green line shows the selected optimal voltage.

As can be seen in fig. 59 with the chosen optimal energy resolution voltage of 359 V stays within the tolerance band for all energies below 1 GeV.
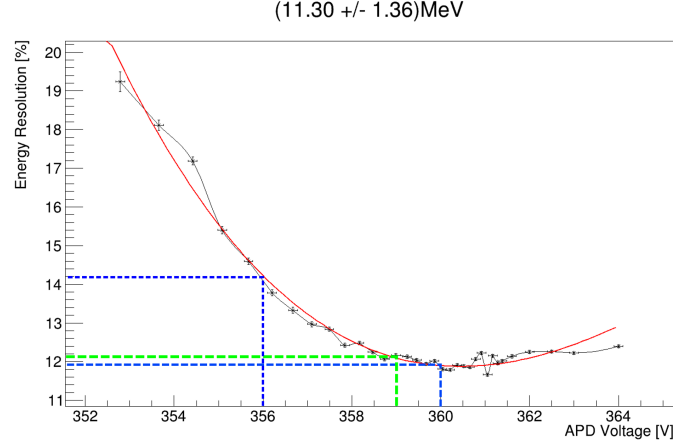
Figure 60: Optimal energy resolution measurement at 11.3 MeV. The optimal energy resolution at ≈ 360 V is indicated as well as the energy resolution for the lower limit at 357 V. The green lines show the energy resolution for the selected optimal working point.

As can be seen in fig. 60, even at the lower limit of 356 V, the resolution loss does not exceed roughly 2.2% at the lowest energy.

5.2 Evaluation of the Recommended Gain

Measurements concerning the energy resolution have already been done for two $\bar{\mathrm{P}}$ANDA prototypes, the PROTO-60 and the PROTO-120. Both are supposed to simulate part of the barrel calorimeter and were used to improve the response and the readout electronics.

The parametrized energy resolution in % for the PROTO-60 can be described by[3]:

$$\frac{\sigma}{E} = \left(\frac{0.25\%}{E/\mathrm{GeV}}\right) \oplus \left(\frac{1.86\%}{\sqrt{E/\mathrm{GeV}}}\right) \oplus 1.46\% \tag{49}$$

The parametrized energy resolution in % for the PROTO-120 can be described by[1]:

$$\frac{\sigma}{E} = \left(\frac{0.16\%}{E/\mathrm{GeV}}\right) \oplus \left(\frac{2.46\%}{\sqrt{E/\mathrm{GeV}}}\right) \oplus 2.32\% \tag{50}$$

For values of the utilized setup, most resolutions were calculated from the fitted functions. Since the fits were mostly done for the best minimal energy resolution, the functions could not be used to calculate the values for $M_{DC} = 150 \equiv 346.507$ V for every energy measurement. Therefore, where the values could not be calculated, they were were extrapolated, as can be seen in fig. 71. For 1.869 GeV however, the values for the optimal gain could neither be calculated nor extrapolated, as data points were missing for higher bias voltages.

Energy equiv.[MeV]	$(\sigma/E)_{gain150}[\%]$	$(\sigma/E)_{V=359\,V}[\%]$	$(\sigma/E)_{PROTO60}[\%]$	$(\sigma/E)_{PROTO120}[\%]$
11.30 MeV	43.2	12.1	28.5	27.2
36.35 MeV	8.0	5.1	12	13.8
58.83 MeV	5.4	3.9	8.9	10.8
107.12 MeV	3.6	2.9	6.3	8.0
272.48 MeV	2.7	2.4	4.0	5.3
558.69 MeV	1.0	0.9	2.9	4.0
1869.47 MeV	0.4	no data	2.0	2.9

Table 5: Overview of the energy resolutions compared to each other. Pictured is the energy resolution of the setup used for $gain_{DC}$=150, the value for the optimal bias voltage of 359 V as well as the values of the PROTO-60 and PROTO-120.

Since the mesaured energy resolution at M_{DC}=150 is already better than the ones measured with the PROTO-60 and the PROTO-120, these measurements cannot be compared. A possible explanation for this behaviour might be that the LED-Pulser already has a better resolution than "real" PWO-II scintillation light would have. Also, the PROTO-60 used an older iteration of the Hamamatsu LAAPDS as well as different preamps[3].

(a)   (b)
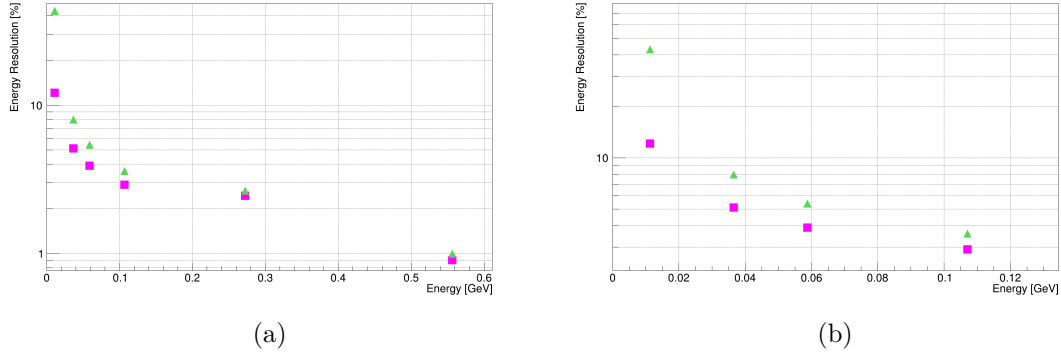
Figure 61: Measured energy resolution in % plotted against the energy equivalent in GeV up to 0.6 GeV. Green points are for $M_{DC} = 150$ and the pink points are for the proposed optimal bias voltage

As can be seen in fig. 61b and in table 5, the energy resolution can be improved significantly in the lower energy regions. Especially for the lowest energy the optimized setting can improve the energy resolution by over absolute 30%.
The bias optimum voltage of 359 V corresponds to a DC gain of approximately 499.6.

5.3   Considering the Dynamic Energy Range of the Barrel EMC

Due to the limited dynamic range of the radout equipment, one has to take into consideration the maximum expected energy inside the barrel EMC. Depending on the polar angle of the crystal, the highest expected energy can range from few hundred MeV to a few GeV. At the most most forward region of the barrel an energy maximum of 7.3 GeV is expected. If the barrel is supposed to be operated at a homogeneous gain, the low gain branch has to cover the equivalent of at least 7.3 GeV[2].
The angular energy distribution can be seen in fig 62.
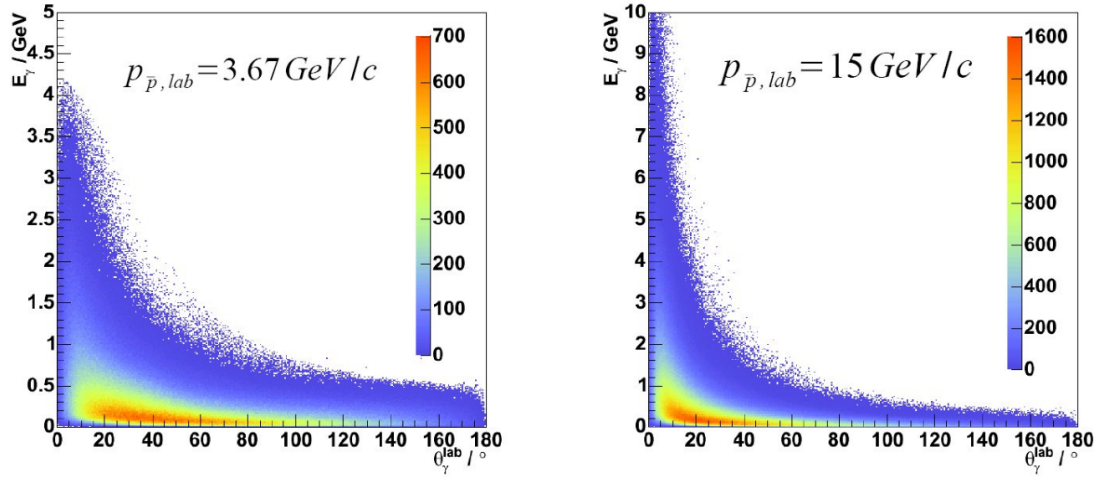
Figure 62: Angular dependance of the photon energy distribution plotted against the angle in the laboratory system[12].

5.3.1 Energy Range of the Utilized Setup

With the setup used, the dynamic range of the SADC as well as the amplification of the buffer have an influence on the dynamic range besides the range of the APFEL ASIC. Since the design for the buffer is not settled yet, these settings can still be ajdusted to fit the needs of the barrel EMC.

As can be seen in ch. 3.6, table 3 the low gain branch for the highest applied voltage (and therefore gain) can handle up to at least 558.69 MeV, which means that for lower voltages the low gain branch is at least able to handle approximately 560 MeV. When talking about optimum gain settings, the needed dynamic range has to be considered.

In order to extrapolate the measurements with the low gain branch, one can look at the measurements for an energy equivalent of 272.47 MeV. This value was chosen from the low gain measurements arbitrarily.

Because the amplitude is proportional to the energy, the amplitude at 7.3 GeV can be extrapolated as follows:

$$A \propto E \leftrightarrow \frac{A(E_1)}{A(E_2)} = \frac{E_1}{E_2}, \tag{51}$$

$$A(7.3\,\mathrm{GeV}) = \frac{7300\,\mathrm{MeV}}{272.47\,\mathrm{MeV}} \cdot A(272.47\,\mathrm{MeV}). \tag{52}$$

When focusing on the energy resolution in the low energy regions, the optimal voltage was above 355 V. However, when comparing with the energy resolution measurement at 272.47 MeV, the signal would already be in saturation at 7.3 GeV for a voltage of 350.598 V. This corresponds to a gain of 200 for the DC characterization.
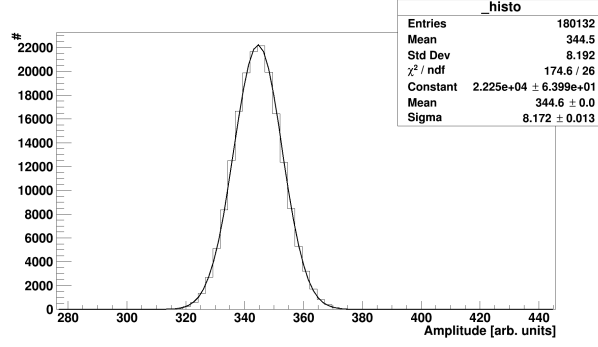
Figure 63: Pulse height for a bias voltage of 350.598 V at 272.47 MeV.

$$A(7.3\,\mathrm{GeV}) = \frac{7300\,\mathrm{MeV}}{272.47\,\mathrm{MeV}} \cdot 344.6 = 9234 \tag{53}$$

The next lower voltage which was measured was at a DC characterization gain of 150.
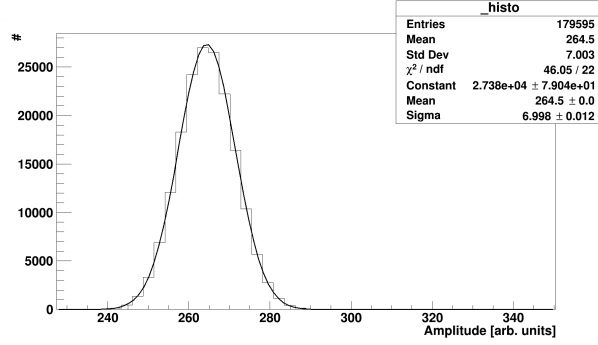
Figure 64: Pulse height for a bias voltage of 346.402 V at 272.47 MeV.

$$A(7.3\,\mathrm{GeV}) = \frac{7300\,\mathrm{MeV}}{272.47\,\mathrm{MeV}} \cdot 264.5 = 7086.2 \tag{54}$$

For bias voltages in between these measurements no statement can be made, but as mentioned before, if the gain is set to a lower value, the reslution loss for low energies is quite high.

The maximum measurable energy can be calculated as follows:

$$\frac{A(E_1)}{A(E_2)} = \frac{E_1}{E_2} \leftrightarrow E_{max} = \frac{A_{max}}{A} \cdot E \tag{55}$$

Since no measurements were made at the selected optimal bias voltage of 359 V a measurement for the next higher bias voltage of 360.038 was chosen as reference. The amplitude of the chosen measurement can be seen in fig. 65.

The maximum amplitude of the linear response region is 7500 a.u.. This gives a maximum energy of 2145 MeV.

$$E_{max} = \frac{7500}{952.5} \cdot 272.47\,\mathrm{MeV} \approx 2145\,\mathrm{MeV}. \tag{56}$$
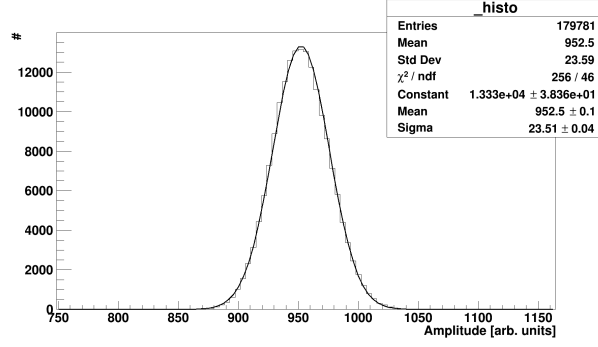
Figure 65: Pulse height for a bias voltage of $360.038\,\mathrm{V}$ at $272.47\,\mathrm{MeV}$.

5.3.2 Energy Range of the APFEL-ASIC

For the $\bar{\mathrm{P}}$ANDA-detector the dynamic range of the ASICs is of utmost importance. The maximum input charge of the APFEL is at $8.5\,\mathrm{pC}$[10], which means signals that produce a higher charge cannot be measured.

The light yield of PWO-II crystals at room temperature is 17 to 20 $\frac{\mathrm{photons}}{\mathrm{MeV}}$[12]. Due to the increase in light yield being

$$\frac{\partial \mathrm{LY}}{\partial\,^\circ\mathrm{C}} = 0.3 \tag{57}$$

at room temperature. The light yield at -25°C would be

$$\Delta \mathrm{LY} = \int_{-25}^{18} 0.3 \, dt = 12.9 \leftrightarrow \mathrm{LY}(-25^\circ\mathrm{C}) = (20 + 12.9)\frac{\mathrm{photons}}{\mathrm{MeV}} = 32.9\frac{\mathrm{photons}}{\mathrm{MeV}}. \tag{58}$$

The higher measured value is used, since the maximal input charge is of importance.
Because the light yield was measured with photodiodes with a quantum efficiency of 20%, the actual number of photons should be 5 times higher. This means the expected LY should be at around $164.5\ \frac{\mathrm{photons}}{\mathrm{MeV}}$. This corresponds to the approximation made by [16] with the light yield of lead tungstate being around 150 - 200 $\frac{\mathrm{photons}}{\mathrm{MeV}}$ at -25 °C.
Moreover, since the active area of the LAAPDs is much schmaller than the front face of the crystal, not all photons will be collected.

$$\frac{\mathrm{photons}}{\mathrm{MeV}}_{LAAPD} = \frac{A_{LAAPD}}{A_{PWO-II}} \cdot LY = 200\ \frac{\mathrm{photons}}{\mathrm{MeV}} \cdot \frac{6.8\,mm \times 14\,mm}{(21.28\,mm)^2} = 42.05 \approx 42\frac{\mathrm{photons}}{\mathrm{MeV}} \tag{59}$$

With a typical quantum efficiency of 70% the expected number of photoelectrons should be

$$\frac{e^-_{ph}}{\mathrm{MeV}} = 42\frac{\mathrm{photons}}{\mathrm{MeV}} \cdot 0.7 = 29.4\ \frac{e^-}{\mathrm{MeV}} \approx 29\ \frac{e^-}{\mathrm{MeV}}, \tag{60}$$

which means the ASIC has to deal with a input charge of

$$\frac{Q_{input}}{MeV} = 29\ \frac{e^-}{MeV} \cdot 1.602 \cdot 10^{-19}\,C \approx 4.6 \cdot 10^{-6}\ \frac{pC}{MeV}. \tag{61}$$

Because the gain of the LAAPD also amplifies the signal, the expected input charge would be

$$\frac{Q_{input}}{MeV} = 4.6 \cdot 10^{-6}\frac{pC}{MeV} \cdot \mathrm{M} \tag{62}$$

The maxmimum energy expected in the barrel calorimeter is at $7.3\,\mathrm{GeV}$[2], which means the maximal permissable gain is:

$$M_{max} = \frac{Q_{max}}{\frac{Q_{input}}{\mathrm{MeV}} \cdot 7300\,\mathrm{MeV}} = \frac{8.5\,\mathrm{pC}}{4.6 \cdot 10^{-6}\,\frac{\mathrm{pC}}{\mathrm{MeV}} \cdot 7300\,\mathrm{MeV}} \approx 253 \qquad (63)$$

These calculations are valid for an AC gain. Since the $\bar{\mathrm{P}}$ANDA screening process measures the DC gain, the actual dynamic range will differ. The difference will give a sligthly increased dynamic range.

For the proposed setting of $359\,\mathrm{V}$ which corresponds to a DC gain of $499.6 \approx 500$, the maximum measurable energy is at

$$E_{max} = \frac{Q_{max}}{\frac{Q_{input}}{\mathrm{MeV}} \cdot M} = \frac{8.5\,\mathrm{pC}}{4.6 \cdot 10^{-6}\,\mathrm{pC} \cdot 500}\,\mathrm{MeV} = 3695.65\,\mathrm{MeV} \approx 3.7\,\mathrm{GeV}. \qquad (64)$$
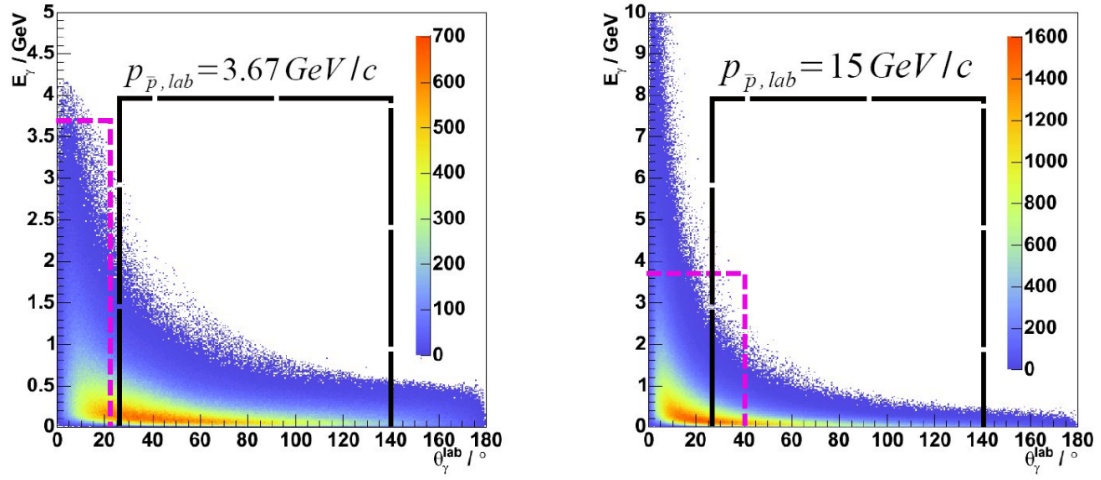
Figure 66: Angular dependance of the photon energy distribution plotted against the lab angle Θ[12]. The pink dotted line indicates the maximum measurable energy and therefore the minimal angle for the proposed setting of gain 500. The black box indicates the angles covered by the calorimeter (22° - 140°)[12].

As can be seen from fig. 66, depending on the beam energy, the optimum value can be set for at least every crystal above an angular positon of 22° - 40°. For energies above approximately $4\,\mathrm{GeV}$ and smaller angles, a lower bias voltage would have to be applied in order to use the full dynamic range. This means the proposed value covers alomst the complete angular range within the barrel EMC.

However, as can be seen from the caluclations with the setup used, the permissable range also depends on the utilized buffer and the dynamic range of the SADC (which is slightly smaller than the one of the APFEL ASIC). For a more correct statement, an AC characterization would have to be used in oder to calculate the maximum energy.

5.4 Effects of Radiation Damages on the Energy Resolution

Because the crystals will be exposed to high energy radiation, radiation damage will occur over time. This leads to a loss in yield light depending on the dose.
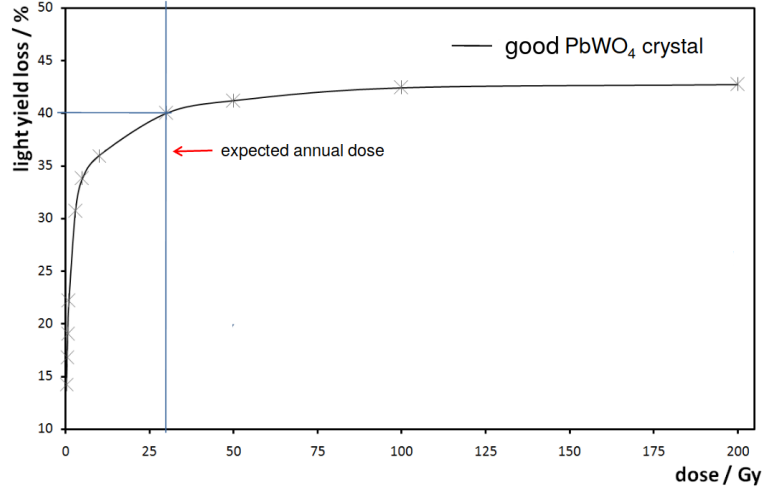
Figure 67: Light yield loss in percent plotted against the radiation dose in Gray with an indication of the expected annual dose for $\bar{\text{P}}$ANDA for one of the better PWO-II crystals, in case of no foreseen annealing[7].

As can be seen in fig. 67 the light yield drops significantly for the firstfew grays and then the light yield loss saturates at approximately 43%. This means the light signals of the crystal will get significantly weaker over time. This has an effect on the energy resolution. Because the measurements were done using a set intensity, the scale of the x-axis seen in fig. 59 will be compressed. This means the optimal bias voltage in terms of energy resolution will be shifted to higher bias voltages for every energy, due to weaker signals. The dynamic range will in increase in MeV via radiation durages.

This favours a higher APD gain close to the limit of the needed dynamic range in the beginning of operation.

5.5 Conclusion

As can be seen from the measurements, huge improvements can be made for the energy resolution when utilizing an optimized gain, especially in lower energy ranges.
The proposed gain, deduced from the measurements done with the LED-pulser, is for the utilized LAAPD at a bias voltage of $359\,\mathrm{V}$ which corresponds to a gain of roughly 500 (measured under continuous illumination).
If this gain is used, the energy resolution for the lowest measured energy can be improved by over 30% compared to a DC gain of 150. Additionally, the energy resolution does not seem to worsen compared to $\mathrm{M}_{DC}=150$ at higher energies.
Lower energies have a higher impact on the considerations for optimal energy resolution than higher energies, since the gain changes more drastically in higher bias voltage regions than in the lower voltage regions. The change in energy resolution is therefore more severe the higher the bias voltage is.
Because of the limited dynamic range of the APFEL ASIC, the angular dependance of the maximum expected energy for the crytsals should be taken into consideration as well. At least for energy resolution purposes, it could therefore be useful to adjust the gain depending on the angular position of the crystal.
For the proposed setting, every crystal with an angular position above 40° can be operated at $M_{DC} = 500$ even with highest beam momenta.
However, because there is a difference in the gain to voltage relation under continuous illumination(DC) and pulsed illumination(AC), one should consider that the actual dynamic range might be a higher than the calculated one, since it was calculated for the AC gain, but the screening process for $\bar{\mathrm{P}}$ANDA involves the DC gain.
Especially for statements about the dynamic range, the AC is important and should therefore be considered.

5.6 Outlook

The in situ characterization of the utilized LAAPD should be finished, in order to make a correct statement about the dynamic range. Since the angular positions, which can be operated at the proposed gain, do not cover the full angular spectrum of the barrel EMC for higher beam momenta, a further study taking into account the constrains on the dynamic range as well as the energy resolution should be conducted.
Since the optimal resolution does not only depend on the LAAPD noise but also the electronic noise of the readout equiptment, one has to think about whether the finished detector will be able to have a noise floor of only $0.25\,\mathrm{MeV}$ for a single module. With higher noise the optimal gain moves to higher values, which has to be taken into consideration.
Lastly, the measurements were done with an undamaged crystal. Since resolution losses are to be expected with radiation damage, it would be interesting to characterize the optimal energy resolution behaviour for damaged crystals, since the optimal settings will most likely shift to higher gain values.

6 Appliance
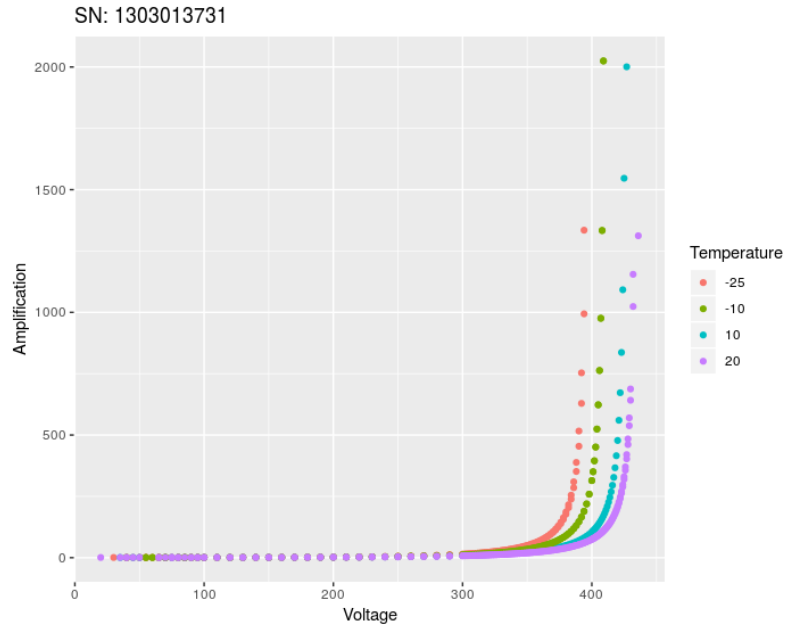
Figure 68: Dependancy of the APD gain on the temperature, plot supplied by [14].
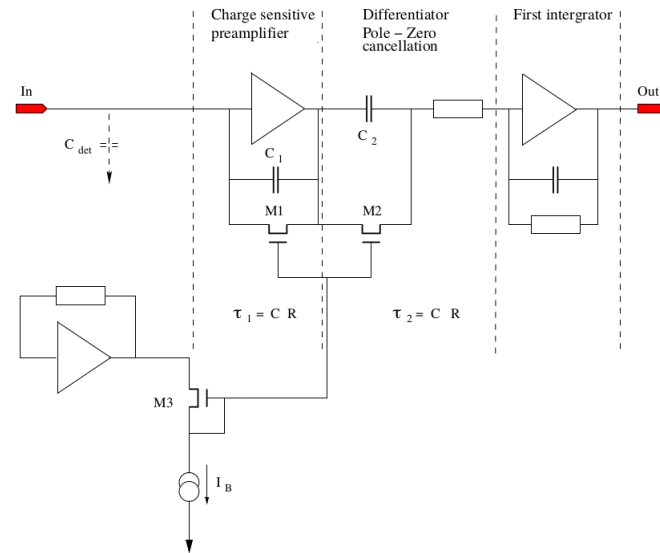
Figure 69: Circuit diagram for the charge sensitive amplifier and the first shaper stage of the APFEL ASIC, taken from [11].
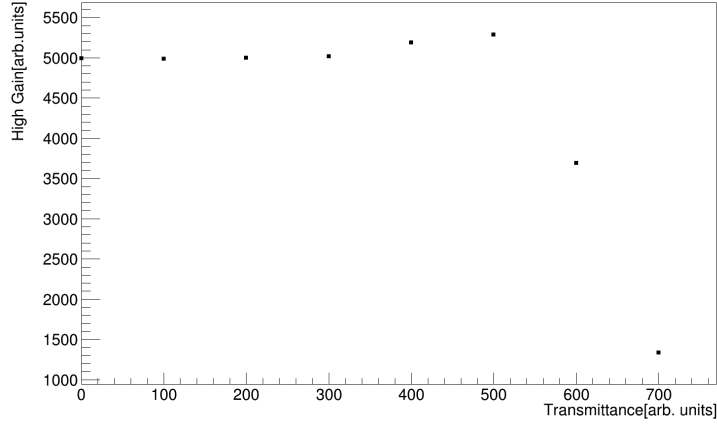
Figure 70: Response of the high-gain LAAPD channel at a set voltage of 361 V at room temperature against the set values for the transmittance in arbitrary units.
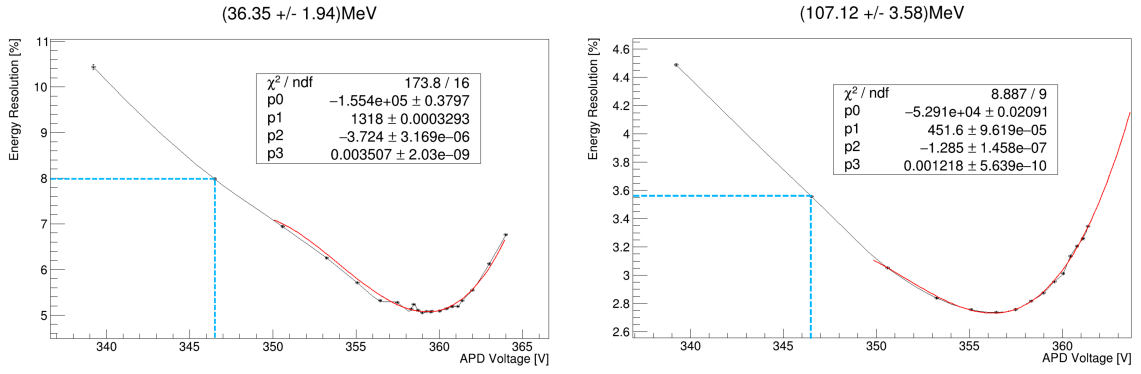
(a) Extrapolation for 36.53 MeV for the resolution at gain 150.

(b) Interapolation for 107.12 MeV for the resolution at gain 150.
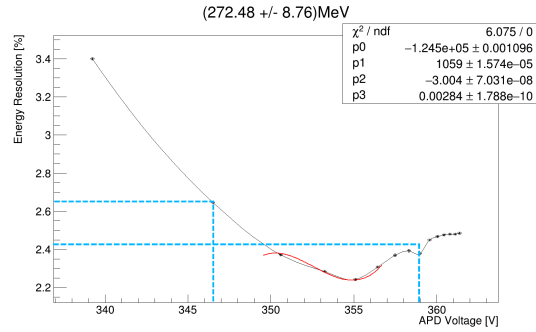
(c) Interapolation for 272.48 MeV for the resolution at gain 150 and at the optimal setting.

Figure 71: Interapolation energy resolutions for different energies.

List of Figures

- **Figure 46, page 37**: Energies measured with a high gain amplification of 32 at a bias voltage of 361.384 V. The number of counts is plotted against the pulse height.
  Figure 46a: 11.3 MeV
  Figure 46b: 36.5 MeV
  Figure 46c: 58.8 MeV

- **Figure 47, page 38**: Energy measured with a high gain amplification of 16 at a bias voltage of 361.384 V. The number of counts is plotted against the pulse height.

- **Figure 48, page 39**: Measured energies in the low gain branch at a bias voltage of 361.384 V. The number of counts is plotted against the pulse height.
  Figure 48a: 272.48 MeV.
  Figure 48b: 558.69 MeV.

- **Figure 49, page 39**: Same intensity of the LED-pulser measured for two different bias voltages.

- **Figure 50, page 40**: Highest intensity measured at 349.194 V, with a mean amplitude of 4656 a.u.

- **Figure 51, page 41**:Measurements for the optimal gain resolution. Plotted is the energy resolution in % against the applied bias voltage, including an interpolution through the data points.

- **Figure 52, page 42**: Raw traces of the SADC.

- **Figure 53, page 43**: Selected noise measurements for different energies. A higher energy was selected as well, because M_{DC}=150 (346.507 V) could not be measured at 11.3 MeV.
  Figure 53c: Noise for 58.8 MeV pulses with a bias voltage of 346.507 V.
  Figure 53b: Noise for 58.8 MeV pulses with a bias voltage of 361.348 V.
  Figure 53a: Noise for 11.3 MeV pulses with a bias voltage of 361.348 V.

- **Figure 54, page 44**: Signals for the selected measurements.
  Figure 54a: Signal for 11.3 MeV pulses with a bias voltage of 361.348 V.
  Figure 54b: Signal for 58.8 MeV pulses with a bias voltage of 361.348 V.
  Figure 54c: Signal for 58.8 MeV pulses with a bias voltage of 346.507 V.

- **Figure 55, page 45**: Measurements for the optimal gain resolution. Plotted is the energy resolution in % against the applied bias voltage.

- **Figure 56, page 46**: Optimum bias voltage in terms of energy resolution.

- **Figure 57, page 47**: Optimal bias voltage of the LAAPD plotted against the energy equivalent. The shaded areas indicate the resolution loss tolerance. Due to missing data at 1.89 GeV, the upper limit of the resolution loss tolerance band was deduced from symmetry considerations.

- **Figure 58, page 47**: Optimum gain in terms of energy resolution. The gain was calculated using the DC characterization.

- **Figure 59, page 48**: Optimal energy resolution. The shaded area represents the 0.2% resolution loss tolerance. The red lines show the chosen limits for the optimal voltage and the green line shows the selected optimal voltage.

List of Tables

References

[1] **Optimization of the Front-End electronics of the PANDA Barrel EMC**
Doctoral thesis
Christopher Rosenbaum
September 2016
`http://geb.uni-giessen.de/geb/volltexte/2016/12281`

[2] **Optimization of the Influence of Longitudinal and Lateral Non-Uniformity on the Performance of an Electromagnetic Calorimeter**
Doctoral thesis
Stefan Diehl
2015
`http://geb.uni-giessen.de/geb/volltexte/2016/11998/`

[3] **Measurements and improvements of the response of the $\bar{\text{P}}$ANDA-EMC prototype PROTO 60 to high energetic particles and photons in accelerator experiments**
Doctoral thesis
Markus Moritz
2013
`http://geb.uni-giessen.de/geb/volltexte/2013/10105/`

[4] **The new PWO Crystal Generation and Concepts for the Performance Optimisation of the PANDA EMC**
Doctoral thesis
Tobias Eissner
2013
`http://geb.uni-giessen.de/geb/volltexte/2013/10382`

[5] **Measurements and Simulations on Position Dependencies in the Response of Single PWO Crystals and a Prototype for the PANDA EMC**
Doctoral thesis
Daniel Andres Bremer
2013
`http://geb.uni-giessen.de/geb/volltexte/2014/10582/`

[6] **Analyse des Zerfalls $\psi(2S) \to \chi_{c0}\gamma \to K_S K_s \pi^0 \pi^0 \gamma$ und Entwicklung eines Lichtpulsersystems für das $\bar{\text{P}}$ANDA-EMC**
Doctoral thesis
Christof Motzko
April 2012
`http://www-brs.ub.ruhr-uni-bochum.de/netahtml/HSS/Diss/MotzkoChristof/`

[7] **Construction and Assembly of the Electromagnetic Calorimeter for the $\bar{\text{P}}$ANDA Target Spectrometer**
Talk at the DPG Spring Meeting
Markus Moritz for the PANDA Collaboration
2018

[8] **Backward End-Cap Activities**
Talk at the $\bar{\text{P}}$ANDA Collaboration Meeting 19/2

Oliver Noll
26. June 2019

[9] **Delivery Specification Sheet, Si APD, Type No.S11048**
Hamamatsu Photonics K.K
First Issued Sep 30, 2013
Revision B Mar 2 , 2018
`Doc.No. KQC-B17033`

[10] **Further Development of the APFEL-ASIC fot the PANDA Calorimeter**
P. Wieczorek and H. Flemming
GSI, Darmstadt, Germany
2012
`https://wiki.gsi.de/foswiki/bin/view/EE/APFEL`

[11] **Low noise preamplifier ASIC for the PANDA experiment**
H. Flemming and P. Wieczorek
2011
`JINST 6 C12055`

[12] **Technical Design Report for:$\bar{\text{P}}$ANDA Electromagnetic Calorimeter (EMC) (AntiProton Annihilations at Darmstadt) Strong Interaction Studies with Antiprotons**
for the PANDA Collaboration.
Rainer Novotny *et al.*
08. August 2008
`https://panda.gsi.de/publication/re-tdr-2008-001`

[13] **Characteristics and use of Si APD (Avalanche Photodiode)**
Hamamatsu Photonics K.K
May 2004
`http://neutron.physics.ucsb.edu/docs/Characteristics_and_use_of_SI_APD.pdf`

[14] **Dr. Benjamin Wohlfahrt**
`private communictaion`

[15] **Dr. Markus Moritz**
`private communictaion`

[16] **Dr. Valera Dormenev**
`private communictaion`

[17] **Johannes Bilk**
`private communictaion`

[18] **Official Website of FAIR**
`https://fair-center.de/index.php?id=1&L=1`

[19] **Official Website of the $\bar{\text{P}}$ANDA-Experiment**
`https://panda.gsi.de/`

[20] **Review of Particle Physics**
PDG booklet
M.Tanabashi *et al.* (Particle Data Group)
17. August 2018
`Phys. Rev. D 98, 030001`

[21] **Experimental Techniques in Nuclear and Particle Physics**
Stefaan Tavenier
Springer-Verlag Berlin Heidelberg
2010
`ISBN 978-3-642-00828-3`

[22] **Teilchendetektoren - *Grundlagen und Anwendungen***
Hermann Kolanoski and Norbert Wermes
Springer-Verlag Berlin Heidelberg
2016
`ISBN 978-3-662-45349-0`

[23] **Particle Data Group**
34. Particle Detectors and Accelerators
Revised 2017
`ALICE Collab., ALICE-PUBLIC-2015-004 (2015)`
`http://pdg.lbl.gov/2019/reviews/rpp2018-rev-particle-detectors-accel.pdf`

[24] **High-Energy Particles**
Bruno Rossi
Prentice Hall
December 1952
`ISBN 978-0-133-87324-5`

Selbstständigkeitserklärung

Hiermit versichere ich, die vorgelegte Thesis selbstständig und ohne unerlaubte fremde Hilfe und nur mit den Hilfen angefertigt zu haben, die ich in der Thesis angegeben habe. Alle Textstellen, die wörtlich oder sinngemäß aus veröffentlichten Schriften entnommen sind, und alle Angaben die auf mündlichen Auskünften beruhen, sind als solche kenntlich gemacht. Bei den von mir durchgeführten und in der Thesis erwähnten Untersuchungen habe ich die Grundsätze guter wissenschaftlicher Praxis, wie sie in der ‚Satzung der Justus-Liebig-Universität zur Sicherung guter wissenschaftlicher Praxis' niedergelegt sind, eingehalten. Gemäß § 25 Abs. 6 der Allgemeinen Bestimmungen für modularisierte Studiengänge dulde ich eine Überprüfung der Thesis mittels Anti-Plagiatssoftware.

_____   _____
Datum   Unterschrift